Development of Thermophysical Property Datasets, Benchmark Niyama Results, and A Simulation Qualification Procedure

Kent D. Carlson and Christoph Beckermann[1]

Department of Mechanical and Industrial Engineering

The University of Iowa, Iowa City, IA 52242

Abstract

Casting simulation results are only useful to a foundry if they reflect reality, which requires accurate thermophysical property data for the alloys being simulated. Of particular interest in the present study is simulation Niyama criterion results. The Niyama criterion, a local thermal parameter that is a common output of casting simulation software packages, is commonly used to predict shrinkage porosity defects in steel castings. Unfortunately, there are a significant number of commonly used alloys for which no reliable property data is available. The present study focuses on five such corrosion-resistant alloys: super-austenitic stainless steel CN3MN, duplex stainless steels CD3MN and CD4MCuN, and nickel-based alloys CW6MC and N3M. Casting trials are performed for these alloys to record metal and mold temperatures during solidification and cooling. Initial alloy properties are generated using thermodynamic simulation software. For each alloy, the simulation pouring temperature and the initial properties are adjusted through an inverse procedure, which directs changes to simulation parameters by comparing thermocouple measurements with virtual thermocouple data. Once the pouring temperature and the alloy properties have been modified with this procedure, good agreement is seen between the measured and simulated thermocouple data. Comparing casting trial simulation Niyama results to corresponding radiographs, it is found that visible radiographic solidification shrinkage is found in regions with Niyama values less than about $1.0 - 2.0$ $(°C\text{-sec})^{1/2}$ /mm, which is in agreement with similar findings for other steel and nickel-based alloys. In addition, the present study also describes a simulation qualification procedure developed to determine the validity of a simulation user's Niyama criterion results. The goal of this procedure is to develop sufficient confidence in a user's Niyama criterion results that purchasers may specify minimum Niyama values in critical casting areas, as an additional means of quality assurance. Users seeking qualification for an alloy perform a solidification simulation with the alloy on a standard casting geometry, according to step-by-step instructions. The minimum Niyama value resulting from this procedure is compared to the benchmark result for the alloy. If the minimum Niyama value obtained in the qualification simulation is lower than or equal to the benchmark value, then the practitioner is qualified for that alloy. Otherwise, the practitioner is not qualified for that alloy.

---

[1] Author to whom correspondence should be addressed. Telephone: (319) 335-5681, Fax: (319) 335-5669, E-mail: becker@engineering.uiowa.edu

1. Introduction

Casting simulation is routinely used in modern foundries because many casting problems can be predicted and eliminated through the use of simulation, rather than through time-consuming and potentially expensive trial-and-error casting production. The Niyama criterion[1], a local thermal parameter that is a common output of casting simulation software packages, is commonly used to predict shrinkage porosity defects in steel castings. Previous studies[2-6] indicate that it is a robust parameter that not only predicts the macro-shrinkage that is visible on radiographs, but also smaller micro-porosity that is usually not detectable using standard NDE techniques. The implication of this previous work is that the Niyama criterion values from a casting simulation may be used not only to provide guidance in designing shrinkage-free steel castings, but also as an additional means for qualifying castings for service. By requiring the Niyama values in a region of a casting to be above a certain critical value, the absence of shrinkage and/or leakage defects in that region could perhaps be assured to the customer. This would be similar to setting an ASTM standard x-ray level requirement for a casting.

An important caveat for casting simulation in general, and for the Niyama criterion prediction in particular, is that the results from a simulation are only as good as the casting data that is utilized in the simulation. For a simulation to truly reflect reality, it is necessary to have accurate thermophysical property data for the alloy and mold materials being simulated (in addition to having reasonably accurate boundary and initial conditions).

1.1 Development of Casting Simulation Thermophysical Property Datasets

Adequate thermophysical property datasets have been developed for many common casting alloys and mold materials, based on a wealth of experimental data that has been gathered in the last half-century. However, for many less common alloys (such as many regularly used corrosion-resistant alloys), little or no property data is available, and hence accurate simulation of castings made from these alloys is not possible. With this in mind, foundries were polled to compile a list of corrosion-resistant alloys that are commonly used, for which reliable simulation property data is currently not available. The list was distilled down to five alloys: three stainless steels (super-austenitic CN3MN, and duplexes CD3MN and CD4MCuN) and two nickel-based alloys (CW6MC and N3M). The compositions of these alloys from the casting trials performed for the present study are given in Table 1.

One common method for developing thermophysical property datasets is to utilize thermodynamic simulation software packages. Using information from thermodynamic databases, these packages model multi-component metal alloy solidification to generate a solidification path. The solidification path consists of the mass fractions and compositions of the various solid phases that form as a function of temperature during solidification. This information is then used to determine the latent heat and temperature-dependent data for the specific heat and density. Two different thermodynamic simulation software packages are utilized in the present study: the stainless steels are simulated using the interdendritic solidification package IDS developed by Miettinen et al.[7-8], and the nickel-based alloys are simulated using JMatPro[9]. Many such software packages are commercially available; these two were selected in part because in addition to generating a solidification path and thermodynamic properties, they also produce transport property curves (i.e., thermal conductivity and viscosity) required by casting simulation software. IDS is only applicable to steels, whereas JMatPro can be

applied to a wider range of alloys (including nickel-based alloys). IDS calculates the transient diffusion of solutes within the phases on the scale of the microstructure, and is thus able to account for the effect of back-diffusion on the solidification path and simulate the solid-state transformations that often occur in steels. JMatPro, on the other hand, uses a modified Scheil approximation (i.e., no solute diffusion in solid phases, except for carbon and nitrogen, for which diffusion in the solid is assumed to be complete).

For many common casting alloys, datasets generated by thermodynamic software packages are reasonably accurate. However, for the highly-alloyed metals considered in the present study, property datasets determined from thermodynamic simulation software are not entirely trustworthy. Sometimes, the content of a particular solute is simply out of the range for which the software was designed, or the thermodynamic database on which the software is based is not fully validated for very high solute contents. More often, the accuracy of the modified Scheil approximation or even the diffusion calculations is not known. This uncertainty affects primarily the solidification path (i.e., the solid fraction as a function of temperature) and the evolution of latent heat. The specific heat, density, thermal conductivity, and viscosity are generally less sensitive to potential inaccuracies in the predictions of the thermodynamic software.

In order to generate reliable property datasets for the corrosion-resistant alloys presently of interest, then, it is necessary to collect experimental temperature data that can be used to determine the solidification path and enthalpy-related properties for these alloys. One common method of performing such measurements is differential thermal analysis (DTA), wherein thermocouples are used to measure temperature differences during the heating or cooling of a small (approximately 200 mg[10]) sample of a metal alloy. The nature of these temperature changes indicates different events that occur during solidification and melting. DTA measurements can provide a great deal of useful information for metal alloys[10]. However, due to the small sample size, the cooling rates involved in DTA can be very different from those found in sand castings, which is the casting technique of primary interest here. In reality, the solidification path is a function of the cooling rate. It is nonetheless referred to as a property, including within this text, since it is a part of the property dataset that a casting simulation requires. Virtually all commercial casting simulation software packages assume that the solid fraction is a function of temperature only and independent of the cooling rate. Because the solidification path depends on the cooling rate, it was decided to perform the temperature measurements in actual sand casting trials of the alloys of interest. The castings were plates with a section thickness that is commonly encountered in foundries casting these alloys, such that the data collected in these trials are for typical cooling rates. It is true that sand casting trials in a foundry have some variability and uncertainty associated with them, but even with DTA a complex inverse procedure would be needed to determine the full solid fraction vs. temperature curve[10].

In summary, one objective of the present study is to develop thermophysical property datasets for CN3MN, CD3MN, CD4MCuN, CW6MC and N3M that are accurate for casting conditions commonly encountered for these alloys in foundry practice. The initial datasets are generated from thermodynamic simulation software. Casting trials are performed to collect temperature data that is used to modify the solidification path and enthalpy-related quantities in these datasets. This modification is performed based on an inverse procedure that compares casting

trial thermocouple results with corresponding simulation values; these comparisons direct changes to the properties to bring the measured and virtual thermocouple results into agreement.

It is worth noting that the comparisons between measured and simulated temperature data, utilized in the present work to develop accurate property datasets, have value in and of themselves. While casting simulation is performed routinely, detailed comparisons between measured and predicted temperatures in an actual casting are scarce in the open literature. Issues such as the selection of simulation parameters (e.g., pouring temperature and mold-metal interfacial heat transfer coefficient) are often discussed among simulation users, but are not investigated systematically, as in the present study. A thorough investigation into the effects of the simulation parameters is necessary, since they are generally unknown and their choice will affect the determination of the alloy properties.

1.2 Development of Benchmark Niyama Results and A Simulation Qualification Procedure

It was stated earlier that the Niyama criterion values from a casting simulation might be used as an additional means for qualifying castings for service. Before the Niyama criterion can be used in this manner, however, it is important to establish a method that assures that the Niyama values are predicted in a reliable and reproducible way that does not depend on the casting simulation software itself or its internal or user settings. Ideally, for the same casting alloy, geometry and process, the same Niyama values should be predicted regardless of software package or user. A previous study was performed by the present investigators to determine the consistency of Niyama predictions, through the use of a round-robin casting simulation exercise[11]. Fifteen foundries performed solidification simulations for a common casting geometry, using five different alloys and three different casting simulation packages. It was found that variables such as the simulation package used and the numerical grid selected made only small differences in the final Niyama predictions. However, differences in the thermophysical property datasets for the metal alloy being simulated, as well as differences in the temperature at which the Niyama criterion is evaluated, can significantly affect Niyama predictions. Therefore, if a simulation is to be used for a purchase specification, it must be ensured that a "good" property dataset is used in the simulation, and a common Niyama evaluation temperature is agreed upon.

The other objective of the present study is to develop a standardized approach to the validation of simulation calculations of the Niyama criterion. This approach involves using a standard casting and developing benchmark Niyama results for a range of alloys. In the present study, benchmark results are generated for the five alloys for which thermophysical property data is being developed (steel alloys CN3MN, CD3MN and CD4MCuN, and nickel-based alloys CW6MC and N3M), as well as six other alloys for which reliable thermophysical property data is available (steel alloys CF8M, CN7M and WCB, and nickel-based alloys CW12MW, M35-1 and M30C). To validate a solidification simulation procedure, an organization can conduct a simulation using the solid model of the standard casting and certain specified casting parameters. The Niyama results from the simulation can then be compared with the benchmark results to determine whether the organization's practice may be considered "valid" or "qualified."

In the next section, an overview is given of the data that must be input into casting simulations, along with a brief discussion of the accuracy of this data. Section 3 discusses the casting trials that were performed for this study, and Section 4 describes how characteristic temperature data

was determined from the temperature measurements collected during the casting trials. Section 5 then details how the alloy property datasets were generated and modified based on the thermocouple data. In Section 6, the relationship between the Niyama criterion and solidification shrinkage is described, and the radiographs from the casting trials are compared to the corresponding Niyama results. This gives an indication of the critical Niyama value below which macro-shrinkage (i.e., shrinkage that is visible on a radiograph) can be expected for these alloys. Section 7 then describes the Niyama benchmark results and the simulation qualification procedure. Finally, the results of this study are summarized in Section 8.

2. Casting Simulation Input

Since the present study is concerned with developing property datasets for casting simulation, it is useful to briefly review the governing equations being solved and the input required. All commercial casting simulation software packages are capable of modeling the melt flow during filling of the mold and the heat transfer during the entire casting process. Filling is simulated by solving the relevant fluid flow equations for the liquid metal as it enters the mold, which requires knowledge of the density and viscosity of the liquid metal. In addition, energy balance equations are solved in both the metal and the mold during filling. Solidification during filling is typically neglected. The solution of the energy equations requires knowledge of the densities, specific heats and thermal conductivities of the materials involved, all as a function of temperature. In the present study, all mold properties are taken from material databases supplied with the simulation software (see below).

After filling is complete, solidification and cooling of the casting is simulated. This also involves solving energy balance equations in both the metal and mold, but typically neglects the effect of heat advection by the residual flow of the liquid metal in the mold cavity. Then, the energy equation for the metal, after completion of filling, can be expressed as:

$$\bar{\rho}\left[\bar{c} - L_f \frac{df_s}{dT}\right]\frac{\partial T}{\partial t} = \nabla \cdot \left(\bar{k}\nabla T\right) \qquad (1)$$

where T is the metal temperature, t is time, and f_s is the solid mass fraction (i.e., $f_s = 0$ if the metal is locally all liquid, and $f_s = 1$ if it is all solid). The use of the total derivative in the term df_s/dT implies that the solid fraction is assumed to be a function of temperature only. The density, specific heat and thermal conductivity of the metal are denoted by $\bar{\rho}$, $\bar{c}$ and $\bar{k}$, respectively. The overbar is used to emphasize that these properties are mixture quantities that depend on the amount of each phase present, in addition to temperature. The term L_f represents the latent heat of fusion per unit mass, which is assumed to be constant over the solidification temperature range. The quantity in square brackets on the left side of Eq. (1) has two terms: the first term accounts for the sensible heat, and the second accounts for the latent heat. This bracketed quantity is often referred to as the effective specific heat:

$$c_{eff} = \bar{c} - L_f \frac{df_s}{dT} \qquad (2)$$

Note that the latent heat term in Eq. (2) is only non-zero while solidification is occurring, since $df_s/dT = 0$ in fully liquid and completely solidified metal. The negative sign in Eq. (2) is the result of df_s/dT being negative during solidification; the release of latent heat generally increases the effective specific heat. All of the metal alloy properties required for casting simulation, including the solid fraction-temperature relation, are generated by thermodynamic simulation software packages. The predicted values for the density, thermal conductivity and, for the most part, specific heat are assumed to be reasonably accurate. The focus in the present study is on verifying and improving the accuracy of the solidification path and the latent heat predicted by the thermodynamic software.

In addition to supplying property data to the simulation, it is also necessary to provide initial temperatures for the metal and the mold. The initial mold temperature is easily determined from sand thermocouple data, but the initial metal temperature (i.e., the simulation pouring temperature) is generally not well known. The simulation pouring temperature represents the temperature of the metal stream as it enters the mold cavity. Typically, temperatures are taken in the furnace, and the metal temperature drop going from the furnace to the ladle to the mold is estimated by a rule of thumb. Even if a temperature measurement is taken in the ladle immediately prior to pouring, the metal stream cools significantly before it reaches the mold cavity. However, by comparing measured metal temperature readings with corresponding simulated values, it is possible to determine the correct simulation pouring temperature. This will be explained in Section 5.

Finally, to solve the governing equations for fluid flow and heat transfer in a casting simulation, it is necessary to provide boundary conditions. The average flow rate of the metal entering the mold is determined from the metal inlet area and the total pouring time. The heat transfer between the mold and the environment and between the top of the riser and the environment are modeled using default settings in the casting simulation software utilized in the present study; the default mold-environment heat transfer boundary condition assumes natural convection, and the default riser top-environment boundary condition assumes hot topping is used, and that heat transfer occurs due to natural convection and radiation. Both of these boundary conditions are reasonable (and have a relatively minor effect on the present results). The most important boundary condition that must be specified is the mold-metal interfacial heat transfer coefficient (IHTC). The choice of the IHTC used in the present study is investigated in detail in Section 5.

3. Casting Trials

The casting trials were performed at Stainless Foundry & Engineering, Inc. Two 1 x 8 x 20 in. (2.54 x 20.32 x 50.8 cm) plates were cast from each alloy, with one plate cast per mold. For each alloy, the plates were poured sequentially from the same heat and ladle. The 1 in. (2.54 cm) plate thickness was selected because it is a typical section size for castings made from these alloys. The plates were end-gated beneath a 4 in. (10.2 cm) diameter end riser. A schematic of the casting configuration is shown in Fig. 1. The molds were all made from phenolic urethane no bake (PUNB) sand. However, there was one notable addition: in the CD3MN molds, there was a layer of chromite sand approximately 1 in. (2.54 cm) thick surrounding the plate. This is a standard practice for this alloy at the casting foundry, so it was automatically done when the mold was made, even though it was not requested.

In each mold, temperature measurements were made using two K-type TCs in the sand (TC-U and TC-D in Fig. 1), and two B-type (Pt-6%Rh – Pt-30%Rh) TCs in the plate (TC-L and TC-R in Fig. 1). The heights above the plate of the K-type TCs, h_1 and h_2, were targeted to be 2 in. (5.08 cm) and 1 in. (2.54 cm), respectively; the actual heights, which varied somewhat, were recorded so that the virtual TCs in the simulations would be in the correct locations. The B-type TC's were constructed by encasing 0.010 in. (0.254 mm) diameter B-type TC wires in a two-hole alumina ceramic tube, and then inserting this assembly into a 6 in. (15.2 cm) long closed-end fused quartz tube. Most of the B-type TCs utilized quartz tubing with an outer diameter (OD) of 0.236 in. (6 mm), but three TCs used 0.157 in (4 mm) OD quartz tubing. The three smaller OD TCs, which have a significantly faster response time than the larger OD TCs, were created to determine whether or not such small diameter TCs would endure the filling and solidification process. A photograph of one of the 0.157 in (4 mm) OD TCs is shown in Fig. 2. The K-type and B-type TCs were connected to a PersonalDaq/3005[12] portable data acquisition system, running DASYLab®[13] data acquisition software.

The casting trials were very successful, in that none of the twenty B-type TCs failed during data acquisition (which is a vast improvement over the 25% failure rate the present authors encountered in a previous casting trial[4]). In particular, all of the 0.157 in (4 mm) OD TCs survived, indicating that such small TCs are indeed a viable option for such experiments. Note that the TCs in the present study were intentionally oriented such that during filling, the inflowing metal would meet the TCs "head-on", at the minimum TC cross-section. If the TCs were oriented such that the inflowing metal stream met a significant length of the quartz tube in cross-flow, for example, it is possible that the force of the metal wave could break the TC.

An example of the temperature vs. time curves generated from the TC data is shown in Fig. 3, for CN3MN. The two plates are denoted as "A" and "B." Note the excellent agreement between the two TCs in each plate. The difference in temperatures between the two plates during cooling is the result of the difference in the pouring temperature for each plate. Fig. 3 is a representative result from the casting trials; similar TC agreement was seen for all alloys studied.

4. Determining Characteristic Temperatures from Thermocouple Data

Taking the time derivative of the temperature curves shown in Fig. 3 produces corresponding cooling rate vs. time curves for each TC. As discussed below, cooling rate data can be used to identify different events that occur during solidification and cooling. Rather than plotting both temperature and cooling rate as functions of time, time can be eliminated from consideration, and the cooling rate can simply be plotted as a function of temperature, as shown for CN3MN in Fig. 4. Initially, the metal is completely liquid, and heat transfer from the metal into the sand mold causes the metal to cool. However, when the liquid metal reaches the liquidus temperature (T_{liq}) and solidification begins, a significant amount of latent heat is released and the cooling of the metal temporarily slows, which creates a local minimum in the cooling rate. This sharp minimum in the cooling rate is identified as the liquidus temperature in Fig. 4. No significant supercooling of the liquid below the liquidus temperature, and the associated temperature recalescence after nucleation, was observed in the present experiments. Below the liquidus temperature, the cooling rate begins to rise as solidification proceeds. The cooling rate reaches a local maximum at the

solidus[2] temperature (T_{sol}), when solidification is complete and the release of latent heat terminates. The solidus temperature is also indicated in Fig. 4. Any kinks in the cooling rate curve indicate the formation of additional solid phases. A secondary solid phase is seen in Fig. 4, where there is a small inflection in the curves near the liquidus temperature. This may indicate the formation of carbides. Note that there is good agreement among all four thermocouples in the values of the characteristic temperatures; similar agreement is seen for the other alloys as well, lending validity to the characteristic temperature values. Note in Fig. 4 that the two plates ("A" and "B") had slightly different cooling rates, which is caused by the pouring temperature being different for the two castings. Nonetheless, the characteristic temperatures are in close agreement. Finally, note that the liquidus temperature is also visible in the upper left of Fig. 3, seen as a plateau in the temperature curve. However, the solidus and other characteristic temperatures are not typically visible in temperature vs. time curves.

Measured cooling rate vs. temperature curves for the two duplex stainless steels (CD3MN and CD4MCuN) are given in Figs. 5 and 6. Unlike Fig. 4, it is seen that the cooling rates do not decrease to a minimum and then increase to denote the liquidus temperature. This is because the pouring superheats in these two alloys were not as high as in the other alloys, and by the time the TCs heated up after first being immersed in liquid metal, the metal surrounding the TCs had already cooled to the liquidus temperature and solidification had begun. It was determined that the maximum TC temperatures recorded in these alloys are very close to the liquidus temperature because the plateau-like behavior noted in Fig. 3 for CN3MN is also seen in the temperature vs. time curves for CD3MN and CD4MCuN (see, for example, the measured temperature curves in Figs. 15 and 16 below). This indicates that the maximum TC temperatures recorded are essentially the liquidus temperatures of these alloys. Also, despite differences in the pouring temperatures of the two plates of each alloy, the maximum temperatures from the four TCs for each alloy only differed by 2°C for CD3MN and by 3°C for CD4MCuN. Thus, for each alloy, the maximum of the four TC readings was taken as the liquidus temperature. As in Fig. 4, Figs. 5 and 6 indicate that a secondary solid phase forms during solidification, just below the liquidus temperature. The solidus temperatures can also be easily identified. However, Figs. 5 and 6 also show an additional characteristic temperature that did not occur in Fig. 4. Unlike CN3MN, which solidifies as austenite and remains austenite down to room temperature, the duplex steels solidify as ferrite, and then at some temperature below solidus, about half of the ferrite begins to undergo a solid-state transformation into austenite. The approximately 50% ferrite – 50% austenite final structure is why these stainless steels are termed "duplex." The latent heat release associated with the beginning of the ferrite-to-austenite phase change causes a local minimum (or at least a significant inflection point) in the cooling rate curves; this is denoted in Figs. 5 and 6. The end of this transformation is subtle enough that it cannot be reliably detected in the cooling rate curves.

The measured cooling rate vs. temperature curves for the two nickel-based alloys are shown in Figs. 7 and 8. Note that the cooling rate scale in these figures is different than the scale used for the steels, because the cooling rates in the nickel-based alloys are smaller than in the steels. As with CN3MN, the liquidus for these two alloys is captured as a sharp minimum in the cooling rate curve, and the maximum in the cooling rate below liquidus denotes the solidus. As with all

---

[2] The term "solidus" is used here to denote the temperature at which the alloy is 100% solidified.

three steels, a secondary solid phase forms during solidification, just below the liquidus temperature. However, for the two nickel-based alloys, a third solid phase is also observed to form during solidification. This tertiary solid phase causes a relatively pronounced and sharp local minimum in the cooling rate curves for CW6MC (see Fig. 7), and it causes an additional inflection in the cooling rate curves for N3M (see Fig. 8).

The characteristic solidification and phase transformation temperatures denoted in Figs. 4 – 8 are given in Table 2. The uncertainty associated with each value is due to small variations in the cooling rate vs. temperature curves among the four thermocouples for each alloy. For the twenty characteristic temperatures given in Table 2, the average variation is ±3°C, with no variation being larger than ±5°C. Thus, the measurements can be considered highly reproducible, despite being performed in a foundry setting. Note that this uncertainty does not include the maximum thermocouple error of 0.5%/°C indicated by the manufacturer[14], which is a standard value for B-type thermocouples. For reference, at 1400°C, the maximum error is ±7°C. The latent heat values in the rightmost column in Table 2 were determined in conjunction with simulation, and will be addressed in the next section.

5. Solidification Path and Thermophysical Properties

5.1 Thermodynamic Simulation and Casting Simulation Details

Initial thermophysical property datasets were generated for each alloy, using the compositions listed in Table 1. IDS[7-8] was used for the three steels (CN3MN, CD3MN and CD4MCuN). Because IDS accounts for finite rate solute diffusion, it is necessary to provide information regarding the cooling rate as a function of temperature. This was done using the data shown in Figs. 4 – 6. On each of these temperature vs. cooling rate plots, horizontal lines were drawn across the plots to create 5 – 8 temperature zones, and the average cooling rate in each zone was estimated from the plot. These cooling rate-temperature pairs were then entered into IDS for each corresponding alloy simulation. The initial property datasets for the nickel-based alloys (CW6MC and N3M) were generated using JMatPro[9]. Because JMatPro uses a modified Scheil approximation and does not consider finite rate solute diffusion, cooling rate data is not considered by the program. Because the Scheil approximation is utilized, however, it is necessary to specify a solidification cut-off value. When the liquid fraction reaches the cut-off value, solidification is considered complete. The cut-off values for the nickel-based alloys were adjusted until the predicted solidus temperatures matched the measured values. Note that without the present measurements of the solidus temperature, it would not have been possible to determine an accurate cut-off value.

The initial property datasets produced by the thermodynamic simulation software packages provide temperature-dependent values of the density, thermal conductivity, specific heat and kinematic viscosity of each alloy. These datasets also contain a solidification path and a value for the latent heat; however, the final values of these quantities were determined inversely by comparing measured and simulated data, as explained below. In addition, the IDS datasets for the two duplex steels (CD3MN and CD4MCuN) also predict the ferrite-to-austenite transformation. For both alloys, the predicted ferrite-to-austenite transformation start temperature was in approximate agreement with the measured values listed in Table 2. The final microstructure predicted for both duplex steels was approximately 50% ferrite – 50% austenite,

as expected. No solid-state transition was predicted for CN3MN, which solidifies as austenite and remains austenite down to room temperature.

The liquidus and solidus values predicted by the thermodynamic software packages typically varied by several degrees from the measured values given in Table 2. Because of these discrepancies, small adjustments were made to some of the property datasets for density, thermal conductivity, specific heat and kinematic viscosity of each alloy. This was necessary because particularly at liquidus, sudden changes occur in some of these properties (i.e., if a property is displayed as a function of temperature, such a change would appear as a "kink" in the property curve). Since the measured liquidus and solidus values were used to generate the solidification paths for these alloys (see below), consistency required that these kinks in the property curves occur at the measured temperatures rather than at their simulated counterparts; therefore the kinks were shifted from the predicted temperatures to the measured values.

In order to generate solidification paths and latent heat values for these initial property datasets, the casting trials were simulated using the general-purpose casting simulation software package MAGMASOFT[®][15]. The rigging shown in Fig. 1 was used for the simulations. For each alloy, virtual TCs were placed in locations corresponding to the actual TC locations in the casting trials. The numerical grid used $\Delta x = \Delta y = 4$ mm and $\Delta z = 3.2$ mm, resulting in 8 computational cells through the plate thickness, and a total of about 214,000 cells in the metal. The mold material used to model the PUNB sand molds was FURAN from the MAGMASOFT[®] database. For CD3MN, the chromite sand around the plate was modeled with the MAGMASOFT[®] database CR_SAND. The initial sand temperatures for each alloy were determined from the sand TC readings before the mold temperatures began to rise ($21 - 22$°C). The interfacial heat transfer coefficient between the metal and the sand mold was taken as a constant value of 1000 W/m^2-K. The legitimacy of this choice will be examined shortly. Filling and solidification were simulated for one plate of each alloy. A simulation fill time of 10 s was selected for all alloys; the recorded fill times were all between 9 and 11 s, and previous simulation experience indicates that changing the fill time by ±1 s effects negligible changes in the results.

5.2 CN3MN

For each alloy, the corresponding initial property dataset was input into the simulation, using the solidification path and latent heat predicted with the dataset as initial estimates of those quantities. As discussed in Section 2, the simulation pouring temperature, T_{pour} was an unknown simulation parameter. Fortunately, it is possible to determine the correct simulation pouring temperature by comparing virtual and measured TC readings. Consider CN3MN, as an example. Using the initial IDS property dataset, a simulation was performed for Plate A—the only difference between simulations of Plates A and B are the sand TC locations and the pouring temperature; for simplicity, only one plate of each alloy was simulated. This initial simulation used $T_{pour} = 1540$°C as a first guess of the pouring temperature (the furnace temperature recorded for this alloy was 1598°C). The temperature and cooling rate curves resulting for the right plate virtual thermocouple (TC-R, as shown in Fig. 1c) in this simulation are compared to the measured values from Plate A, TC-R in Fig. 9a. Note that the IDS solidification path used in this simulation has a liquidus temperature 1°C less than the measured value, and a solidus temperature 2°C less than the measurement (see Fig. 10); these small differences are not visible on the temperature scale used in Fig. 9. Both the virtual and real TCs begin to heat at the same

10

time, when metal first comes into contact with them. The virtual TC immediately jumps to the temperature of the surrounding metal, but the real TC has a thermal lag, and it takes about 30 s for this TC to heat up to the temperature of the surrounding metal. For T_{pour} = 1540°C, it is evident in Fig. 9a that the virtual TC reaches the measured liquidus temperature (indicated by the upper dashed line) later than the measured TC. This indicates that the simulation superheat is too high, and thus T_{pour} is lower than this first guess of 1540°C.

With this information, additional simulations were run with the same property dataset, but with different values of T_{pour}. After several iterations, T_{pour} = 1502°C was selected. The resulting temperature and cooling rate curves for TC-R in this simulation are shown in Fig. 9b. With this choice of T_{pour}, the time to reach liquidus in the simulation now agrees with the measurement, indicating that the correct pouring temperature has been determined. Note that this pouring temperature will continue to give the correct time-to-liquidus as changes are made to the latent heat and solidification path, because the time-to-liquidus is primarily affected by properties above the liquidus temperature. Comparing Figs. 9a and 9b, notice that changing the initial temperature noticeably affects the time required to reach the solidus temperature. Some of this can be attributed to the fact that the liquidus is reached sooner in Fig. 9b than in Fig. 9a, but the difference in time-to-solidus is larger than this difference. Reducing the pouring temperature results in less initial energy in the metal when cooling begins, which correlates to slightly faster cooling in the metal overall. This phenomenon is also seen in Fig. 3, where the TC's in Plate B cool slightly faster than those in Plate A, due solely to the difference in the pouring temperatures of these two plates.

While the time to reach liquidus is the same for the simulation and measurement in Fig. 9b, there is still a large discrepancy between the measured and simulated time to reach the solidus temperature (indicated by the lower dashed line). The simulated time-to-solidus is much longer than the measured time, indicating that solidification is proceeding too slowly in the simulation. This is largely because the value of latent heat given by the IDS simulation for CN3MN (L_f = 253 kJ/kg) is too large. To illustrate how changing the latent heat changes the solidification time, Fig. 9c shows the results of a simulation run with T_{pour} = 1502°C, but with the latent heat changed to L_f = 200 kJ/kg. This figure demonstrates that changing the latent heat clearly changes the time the simulation takes to reach solidus. Using L_f = 200 kJ/kg with the initial IDS dataset, the time-to-solidus in the simulation is now the same as the measured time.

Although the simulation times to reach liquidus and solidus in Fig. 9c are now in agreement with the measured values, the simulated and measured temperatures and cooling rates do not agree very well in the solidification range. To bring the temperatures into better agreement during solidification, it is necessary to alter the solidification path. This involves a substantial amount of iteration: adjusting the solidification path, then running a simulation and comparing the new simulation results to the measurements, and using this information to make further adjustments to the solidification path. The results from the simulation with the final modified solidification path (again using T_{pour} = 1502°C) are shown in Fig. 9d. Now, the temperatures and cooling rates during solidification are in very good agreement. Note that the latent heat listed in Fig. 9d has changed from 200 kJ/kg (in Fig. 9c) to 180 kJ/kg. This change in the latent heat required to get agreement in the time-to-solidus is the result of changing the solidification path. The physical explanation for the change in latent heat as the solidification path changes can be understood by

considering Eq. (2): changing the solidification path changes df_s/dT, so in order to obtain the same effective specific heat, the value of the latent heat must change as well.

The final latent heat value determined for CN3MN (180 kJ/kg) is listed in the rightmost column in Table 2. An estimated uncertainty of ± 5 kJ/kg is included with this value. The uncertainty arises because if one compares the measured and simulated temperatures and cooling rates for TC-L in Plate A (the focus thus far has been on TC-R), the simulated and measured times to reach the solidus temperature do not agree exactly. In this case, it is necessary to decrease the latent heat by about 5 kJ/kg to get time-to-solidus agreement. Further slight disagreements are likely to be seen if Plate B is simulated. Hence, an uncertainty is provided with the latent heat values given in Table 2.

It could be fairly stated that the dataset used to generate the results in Fig. 9c is perfectly acceptable, without modification to the solidification path. The agreement between measured and simulated temperatures below solidus is essentially the same as the results with the modified solidification path (Fig. 9d), and the temperature differences seen in the solidification region in Fig. 9c are not that large. Thus, overall temperature prediction with the original solidification path would be reasonable. The motivation behind modifying the solidification path lies in casting defect prediction. Many casting defects (solidification shrinkage, hot tears, etc.) occur near the end of solidification. Accurate prediction of these defects requires an accurate representation of the solidification path in this region. The IDS solidification path is compared with the modified path in Fig. 10. The modified path forms solid faster near liquidus and slower near solidus than the IDS path. The horizontal dashed line near the top of this plot indicates the point where the metal is 95% solidified. The IDS solidification path reaches 95% solid 22°C above solidus, whereas the modified path reaches 95% solid 33°C above solidus. This significantly larger temperature difference with the modified path provides more opportunity for defects to form. In other words, the IDS solidification path may under-predict defects compared to the modified path.

Comparing Figs. 9a and 9d clearly illustrates that this inverse procedure, wherein modifications to the simulation pouring temperature and to the original dataset are made by comparing measured and simulated thermocouple results and then iteratively adjusting the simulated dataset until the results agree, is very effective (if somewhat tedious). To summarize, the inverse procedure involves the following steps:
- beginning with the initial property dataset and a guess for the simulation pouring temperature, adjust T_{pour} until the simulated and measured times to reach liquidus agree;
- adjust L_f until the simulated and measured times to reach solidus agree;
- adjust the solidification path (and L_f again, as necessary) until the simulated and measured temperatures and cooling rates during solidification agree.

5.3 Parametric Study of Interfacial Heat Transfer Coefficients

Before continuing on with the other alloys, the choice of the mold/metal interfacial heat transfer coefficient (IHTC) used in the simulations discussed thus far (taken as a constant 1000 W/m^2-K) is investigated. Fig. 11 shows the measured temperature results (again from CN3MN, Plate A, TC-R), along with corresponding results from three different simulations. The simulations each

used a different constant value of IHTC: one is the simulation from Fig. 9d, with IHTC = 1000 W/m^2-K, one used IHTC = 100 W/m^2-K, and one used IHTC = 6000 W/m^2-K. All three simulations were performed using the modified solidification path shown in Fig. 10. Because the heat transfer from the metal to the mold is different in each of these simulations, the simulation pouring temperature required to get agreement with the time-to-liquidus is different for each simulation: for IHTC = 6000 W/m^2-K, T_{pour} = 1520°C; for IHTC = 1000 W/m^2-K, T_{pour} = 1502°C (as in Fig. 9d); and for IHTC = 100 W/m^2-K, T_{pour} = 1435°C. Similarly, the value of latent heat required to get agreement with the time-to-solidus is also different for each simulation. The differences in the pouring temperature and latent heat between these simulations are depicted in Fig. 12. The pouring temperature is plotted in a more meaningful form, as the superheat (= $T_{pour} - T_{liq}$, where T_{liq} = 1387°C for CN3MN). Data from an additional simulation not shown in Fig. 11, with IHTC = 500 W/m^2-K, is included to clarify the nature of the steep drop in the curves shown in Fig. 12. Note that neither the superheat nor the latent heat changes significantly from 1000 to 6000 W/m^2-K, and that both of these quantities drop rapidly below 1000 W/m^2-K. Returning to Fig. 11, it is seen that there is very little difference in the temperature curves for 1000 and for 6000 W/m^2-K, and that both agree well with the measured temperature curve. This implies that any constant IHTC greater than 1000 W/m^2-K will give results very similar to the 1000 W/m^2-K results; Fig. 12 indicates that higher IHTC values will simply require slightly larger superheats and latent heats to obtain agreement. It also appears from Fig. 11 that 100 W/m^2-K is too small, given that the temperature for 100 W/m^2-K cools too slowly below the solidus temperature. In addition, the superheat and latent heat values shown in Fig. 12 for 100 W/m^2-K are much too small to be realistic.

Further evidence of which IHTC should be used can be found by comparing sand TC measurements. Fig. 13 shows the measured and simulated sand TC temperature curves corresponding to the metal temperatures shown in Fig. 11. Fig. 13a shows the values for TC-U, which was 2.0 in. (5.08 cm) above Plate A, and Fig. 13b shows the values for TC-D, which was 1.1 in. (2.79 cm) above Plate A. As in Fig. 11, the 1000 and 6000 W/m^2-K simulation results agree well with each other and with the measured temperatures. Fig. 13 further indicates that the value of 100 W/m^2-K is too small, as both the TC-U and TC-D temperature measurements are significantly under-predicted using this IHTC.

Finally, the data for TC-D from the Plate A mold is further investigated in Fig. 14, which plots the simulation temperatures at time t = 460 s as a function of IHTC (this time is indicated as a vertical dashed line in Fig. 13b). The measured temperature from TC-D at this time (260°C) is shown as a horizontal dashed line. Using the filling simulation temperature results and final CN3MN property dataset from the base case IHTC = 1000 W/m^2-K simulation (i.e., the simulation with T_{pour} = 1502°C, L = 180 kJ/kg, and the modified solidification path), solidification was simulated with several different values of IHTC. This approach, using the 1000 W/m^2-K filling result and the base case CN3MN property dataset, and just simulating solidification with different IHTCs, was adopted because it would take a great deal of time to perform the iterations required to find the appropriate pouring temperatures and latent heats for a large number of IHTCs, as was done for the simulations with IHTC = 100, 1000 and 6000 W/m^2-K shown in Figs. 11 – 13. The difference this approximation causes is small, however; the values shown in Fig. 14 for 100 and 6000 W/m^2-K only differ from the corresponding values in Fig. 13 by 4% and 1%, respectively. The curve of simulated data in Fig. 14 shows that the 1000 W/m^2-K

result agrees very well with the measured value, and that IHTC values between about 500 and 2000 W/m^2-K give reasonable agreement with the measured sand temperature. Below about 500 W/m^2-K, the predicted sand temperature drops rapidly, indicating that the IHTC is too small. Based on the information in Figs. 11 – 14, the choice of IHTC = 1000 W/m^2-K appears to be quite reasonable, and therefore this IHTC will continue to be utilized for the other alloys.

The conclusion that IHTC = 1000 W/m^2-K gives reasonable results is not surprising; sand casting simulation users at foundries commonly use values in the range of 800 – 1000 W/m^2-K. However, they settled on these values empirically. The present parametric study systematically demonstrates that 1000 W/m^2-K is a reasonable value for steel and nickel-based alloys cast in sand molds, and it also shows the sensitivity of the results to the choice of IHTC. One could argue that in reality the IHTC is a temperature-dependent quantity, and a higher value should be used when the metal is all liquid than when it is solid at, say, 600°C. While this may be true, a constant IHTC is nonetheless effective because the predicted results are insensitive to the IHTC for values above 1000 W/m^2-K, as demonstrated here.

5.4 CD3MN and CD4MCuN

Next, the inverse procedure described in Section 5.2 was applied to the two duplex stainless steels (CD3MN and CD4MCuN). Comparisons between measured thermocouple results and corresponding simulation results are shown in Fig. 15 for CD3MN, and in Fig. 16 for CD4MCuN. Figs. 15a and 16a show results from simulations that used the original, unmodified IDS datasets, and Figs. 15b and 16b show results from simulations that used the final modified datasets. All simulations in Figs. 15 and 16 used the correct pouring temperature. The final latent heat values found for these alloys are listed in Table 2. The original IDS dataset simulation results in Fig. 15a for CD3MN are in fair agreement with the measurements, but the simulation begins to cool too slowly near the end of solidification, and this trend continues below solidus. Excellent agreement between measurement and simulation is seen after the dataset is modified, as shown in Fig. 15b. In contrast to CD3MN, Fig. 16a shows that the original IDS dataset simulation results for CD4MCuN agree poorly with the measured results. The simulation cools too quickly during solidification, and then too slowly in subsequent cooling below solidus. The reason that the original dataset for CD3MN gives somewhat reasonable results, while the original dataset for CD4MCuN gives very poor results, is the large copper content in CD4MCuN. The 3% Cu addition exceeds the allowable IDS range for this alloying element, which is 0 – 1%. In this instance, the extrapolation that IDS performs with the large copper content creates an unrealistic liquidus value and solidification path. Modification of this dataset, however, to correct the solidification range and latent heat, produces excellent agreement between measurement and simulation, as seen in Fig. 16b.

For these duplex steels, additional dataset modification was required to produce the "kinks" seen in the cooling rate curves after solidification is complete, which correspond to the latent heat release during the ferrite-to-austenite transformation. IDS contains a model that simulates austenite decomposition below 1000°C and accounts for the latent heat related to this transformation; however, although IDS simulates the ferrite-to-austenite transformation in terms of phase fractions, it does not account for the associated latent heat release. This latent heat release can be added manually to the thermophysical datasets, by modifying the specific heat curve. Thinking of the specific heat below solidus as an effective specific heat, as introduced in

Eq. (2), adding a peak to the specific heat curve effectively adds the latent heat contribution to the sensible heat predicted by IDS. This has the same form as Eq. (2), except that the latent heat of fusion, L_f, is replaced by a latent heat of ferrite-to-austenite transformation, $L_{fer-aus}$, and df_s/dT is replaced by df_{aus}/dT, the change in austenite phase fraction with temperature. The modified specific heat curves for the duplex steels are shown in Fig. 17, along with the corresponding original IDS specific heat curves. The modified specific heat curves each have a spike, whose peak occurs at the ferrite-to-austenite transition start temperature listed in Table 2. The height of the spikes, and the width of their bases, was determined through the same type of inverse procedure that has been discussed throughout this paper, changing the shape until the simulated cooling rate curves matched the measured values. The spikes seen in the IDS specific heat curves in Fig. 17 are the result of the IDS austenite decomposition model. Even though IDS correctly predicts the phase fractions of ferrite and austenite during the ferrite-to-austenite transformation, the spike that corresponds to austenite decomposition, peaking at about 600°C, still appears in the specific heat curves. This spike was removed in the modified curves, since austenite decomposition does not occur. The slope of the modified curves after the ferrite-to-austenite spike was chosen to match the slope of the IDS curves just below solidus. The decrease in the modified specific heat curves compared with the IDS curves that begins near the end of solidification was determined through inverse analysis. Figs. 15b and 16b show that the modified specific heat curves give good agreement between measurement and simulation below solidus. Although it is not shown in Figs. 15b and 16b, reasonable agreement between simulation and measurement is seen down to about 600°C (where temperature measurement stops), indicating that removal of the peak in the IDS curves was valid.

Considering the specific heat curves in Fig. 17, one might notice that the specific heat curves are smooth in the solidification ranges, and wonder why there are no spikes in these curves to account for the latent heat released during solidification. The reason is that casting simulation packages typically add the latent heat of solidification in separately; the thermophysical property datasets include the latent heat and the solidification path, and so the casting simulation packages use this information to calculate $L_f(df_s/dT)$ in Eq. (2) directly. However, this is only done in the solidification range, and so the latent heat due to solid-state transformations must be explicitly included in the specific heat curves.

5.5 CW6MC and N3M

Finally, the inverse procedure was applied to the two nickel-based alloys (CW6MC and N3M). The TC comparison results for both the unmodified JMatPro dataset simulations and the modified dataset simulations are given in Fig. 18 for CW6MC, and in Fig. 19 for N3M. Again, the final latent heat values found for these alloys are listed in Table 2. The simulated temperature results for CW6MC with the original JMatPro dataset, shown in Fig. 18a, are in relatively good agreement with the measurements. However, comparison between measured and simulated cooling rate curves in the solidification range shows poor agreement. The simulated cooling rate curve only approximately captures the secondary solid phase formation that occurs at about 150 s, and entirely misses the sharp local minimum due to the tertiary phase formation at about 450 s. Once the CW6MC dataset is modified, however, Fig. 18b shows that both the simulated temperature and cooling rate curves give excellent agreement with the measurements. In order to capture the large spike (local minimum) in the cooling rate curve associated with the tertiary

phase formation, it was necessary to put a significant kink in the CW6MC solidification path. The final solidification path for CW6MC is shown in Fig. 20, along with the final solidification paths determined for the other alloys. Notice that the solidification paths for all the other alloys look relatively smooth; aside from the large spike in the cooling rate curve for CW6MC, all the other kinks in the cooling rate curves for these alloys were modeled with subtle changes in the curvature of the solidification paths.

The original JMatPro dataset simulation results for N3M, shown in Fig. 19a, do not agree well with the measured temperatures or cooling rates. The simulated casting cools too fast in the solidification region. The secondary solid phase is again only very approximately modeled by an inflection in the cooling rate curve, and the tertiary solid phase is completely missed. The modified dataset simulation results, shown in Fig. 19b, again show excellent agreement with the measured values.

Finally, the N3M simulation results shown in Fig. 19b are repeated in Fig. 21a, showing a larger temperature range and time scale. As with the duplex steels, an additional modification had to be made to the specific heat curve for N3M, in order to account for a solid-state transformation that can be seen by the kink in the measured cooling rate curve for N3M at about 830°C in Fig. 21a. This transformation (whose value is included in Table 2) is not shown in Fig. 8, because the temperature range in Figs. 4 – 8 (1000°C – 1500°C) was selected to highlight the solidification ranges. The N3M solid-state transformation is the only transformation that is not shown in Figs. 4 – 8. To model this transformation, the N3M specific heat curve was modified below solidus, as shown in Fig. 21b. The modification to the original JMatPro curve was again determined inversely. Note that the JMatPro curve has a peak similar in shape to the modified peak, but occurring at a much lower temperature. It is possible that the JMatPro peak accounts for the same transformation the modified peak is capturing, just over a temperature range that is too low. With this modified specific heat curve, Fig. 21a shows that the simulated temperature and cooling rate curves are in excellent agreement with the measurements.

6. Comparison Between Solidification Shrinkage and Niyama Criterion

The Niyama criterion[1] is a local thermal parameter calculated by simulation software packages that is commonly used to predict feeding-related shrinkage porosity caused by shallow temperature gradients. It is defined as

$$Ny = G \big/ \sqrt{\dot{T}} \tag{1}$$

where G is the thermal gradient, and $\dot{T}$ is the cooling rate. The Niyama criterion is evaluated near the end of solidification, when solidification shrinkage typically forms. Shrinkage porosity is expected to form below some critical minimum Niyama value, where the minimum Niyama value is defined as the lowest Niyama value in the region of interest. The relationship between the minimum Niyama value and shrinkage porosity is shown schematically in Fig. 22. For large minimum Niyama values, no shrinkage porosity is expected. When the minimum Niyama value decreases below a certain critical value (Ny_{micro}), micro-shrinkage (i.e., tiny solidification shrinkage that is not visible on a standard radiographic film) begins to form. As the minimum Niyama value decreases further, the amount of shrinkage increases until another critical value

(Ny_{macro}) is reached. At this point, the amount of shrinkage is sufficiently large that it is termed macro-shrinkage (i.e., visible solidification shrinkage that can be detected by common radiographic techniques). The amount of macro-shrinkage increases as the minimum Niyama value decreases below Ny_{macro}.

The Niyama criterion, as evaluated in casting simulation software, has been found to provide a robust prediction of feeding-related shrinkage. It predicts macro-shrinkage as well as micro-shrinkage not detectable via radiography. Previous studies by the present authors[2-6] indicate that the critical minimum Niyama values shown in Fig. 22 have the following ranges for the steel and nickel-based alloys investigated: $Ny_{macro} = 0.1 - 1.0$ (°C-sec)$^{1/2}$ /mm, depending on the radiographic sensitivity; and $Ny_{micro} = 2.0 - 3.0$ (°C-sec)$^{1/2}$ /mm. The Niyama criterion does not explicitly predict hot spots in a casting, and it does not predict gas porosity or other solidification defects. Thus, the Niyama criterion should not be used as the only method of quality assurance.

As a part of the present investigation, radiographs were taken of each of the plates from the thermocouple casting trials described in Section 3. Using the thermophysical property data developed for each of the five corrosion-resistant alloys studied here, it is now possible to compare Niyama predictions from the simulations of the plate casting trials with the radiographs of the trial plates. These comparisons are shown in Figs. 23 – 27 (one alloy per figure). Each figure compares the radiographs of the two plates of one alloy to the mid-plate Niyama prediction from the casting simulation of one of the two plates of that alloy (the Niyama prediction for the other plate is very similar for all alloys). Below each plate, the radiographic testing (RT) shrinkage level ratings for that plate are provided. The plates in the trials were designed to be long enough to significantly exceed the expected feeding distances, so all plates are Level 4 or Level 5. The thin vertical shadows at the bottom of each plate are the thermocouples. Finally, superimposed on each radiograph are two enclosed curves, which were determined from the corresponding Niyama plot for each alloy. These curves are provided to compare the locations on the radiographs containing visible shrinkage with the Niyama values in these locations. The solid curve encompasses the region on the Niyama plot where $Ny \leq 1.0$ (°C-sec)$^{1/2}$ /mm, and the dashed curve encompasses the region where $Ny \leq 2.0$ (°C-sec)$^{1/2}$ /mm.

Fig. 23 shows the comparison between radiographs and Niyama contours for the super-austenitic stainless steel CN3MN. Note that in both plates, most of the visible shrinkage is confined to the region $Ny \leq 1$. In Plate A, there are definitely a few shrinkage indications that are outside the region $Ny \leq 1$; these indications are encompassed by the curve indicating $Ny \leq 2$. Plate B has only a few minor indications outside the region $Ny \leq 1$, and again these indications are within the region $Ny \leq 2$. Figs. 24 and 25 show the comparisons for the two duplex stainless steels, CD3MN and CD4MCuN. The first thing to note is that the Niyama contours for these two alloys are similar to each other, and different from those for CN3MN. The duplex steel Niyama contours are significantly wider and more rectangular. Also, there is much less difference between the sizes of the $Ny \leq 1$ and $Ny \leq 2$ regions than was seen for CN3MN, indicating that the thermal gradients are steeper in these duplex steels [see Eq. (1)]. For both duplex steels, the visible shrinkage indications on the radiographs are almost entirely contained within the $Ny \leq 1$ curves. Near the risers, there are potentially a few indications outside the region where $Ny \leq 1$. As with CN3MN, these indications are still encompassed by the $Ny \leq 2$ curves. Figs. 26 and 27 show the comparisons for the two nickel-based alloys, CW6MC and N3M. Comparing Fig. 26 to Fig. 23,

it is seen that the Niyama contours for CW6MC look similar to the Niyama contours for CN3MN. By comparing the $Ny \leq 1$ and $Ny \leq 2$ curves in Fig. 23 and Fig. 26, it is seen that both the $Ny \leq 1$ and $Ny \leq 2$ regions for CW6MC are a bit narrower than for CN3MN. At first glance, the Niyama contours for N3M in Fig. 27 may seem different than those in Fig. 23, but this is due to the contours with values of $Ny > 2$ in Fig. 27, which extend all the way to the sides of the plates. Comparing the $Ny \leq 1$ and $Ny \leq 2$ curves on the radiographs in Figs. 23 and 27, however, it becomes evident that these curves are similar for CN3MN and N3M. The $Ny \leq 1$ region in N3M is again a bit narrower than in CN3MN. However, the $Ny \leq 2$ region is very similar (slightly wider in N3M than in CN3MN, in fact). For the nickel-based alloys shown in Figs. 26 and 27, it is also seen that most of the shrinkage indications lie within the region $Ny \leq 1$, and that almost all indications lie within $Ny \leq 2$. Even though the $Ny \leq 1$ and $Ny \leq 2$ curves have different shapes for different alloys, it is evident that most of the visible shrinkage for all the alloys considered here falls within the region $Ny \leq 1$, and that nearly all the visible shrinkage is within the region $Ny \leq 2$. Thus, it seems reasonable to state that the areas on the radiographs that show visible shrinkage correspond to regions where the Niyama values are less than $Ny_{macro} = 1.0 - 2.0$ $(°C\text{-sec})^{1/2}$ /mm. This range is in agreement with findings from similar studies with other metal alloys. It should be noted that Ny_{macro} does not necessarily have to be the same for the stainless steels and the nickel-based alloys; the difference in the alloy base metal can cause differences in thermal gradients, etc., which can change the critical value. However, in the present study, $Ny_{macro} = 1.0 - 2.0$ $(°C\text{-sec})^{1/2}$ /mm seems reasonable for all the alloys considered.

Now that accurate thermophysical property datasets have been developed for the five corrosion-resistant alloys of interest, and the correlation between the Niyama criterion and the presence of radiographic macro-shrinkage has been determined for these alloys, it is time to turn to the other objective of this study: the development of a simulation qualification procedure and the benchmark Niyama criterion results that are to be used for qualification. This is the subject of the next section.

7. Niyama Benchmark Results and Simulation Qualification Procedure

The simulation qualification procedure was developed as the result of a collaboration between the SFSA, the MTI, and the University of Iowa. The procedure is the end-result of a continuation of the work performed for (and the lessons learned from) the Niyama round-robin study[11]. The qualification procedure is described in complete detail at the following SFSA website: http://www.sfsa.org/folio/downloads/MTI. This website is password protected; SFSA members can obtain the user ID and password for the website by contacting the SFSA. The website contains three documents (both as web pages and as downloadable pdfs):

- Casting Simulation Niyama Criterion Qualification: This document provides a complete description of the simulation qualification procedure, along with step-by-step instructions for performing the procedure. The web page includes links to download CAD files for the standard casting geometry that is used for qualification. In addition, this document provides background on the Niyama criterion and its relationship with shrinkage porosity, as well as a discussion of some of the sources of variability in simulation Niyama results.

- Benchmark Results: This contains the benchmark Niyama criterion results for the standard casting in eleven different alloys: CD3MN, CD4MCuN, CF8M, CN3MN,

CN7M, CW6MC, CW12MW, M35-1, M30C, N3M, and WCB. This document also include details of the simulations used to produce the benchmark results.

- Simulation Qualification Record: This is the form that users use to document the qualification exercise and to report the results. The website provides this form as a Microsoft Word document, in addition to html and pdf formats. This form is provided in Appendix A.

The qualification website also contains the alloy thermophysical property datasets that were used to obtain the benchmark results. These datasets are downloadable both as Excel spreadsheets and as MAGMA binary database files. The alloys that are available via the website are: CD3MN, CD4MCuN, CF8M, CN3MN, CN7M, CW6MC, CW12MW, CZ100, M30C, M35-1, N3M and WCB.

The standard casting geometry utilized for the simulation qualification is a valve with a riser in a rectangular mold box, shown schematically in Fig. 28. This is the same casting that was utilized for the Niyama round-robin study[11]. As mentioned above, users seeking qualification must download CAD files for this casting geometry from the SFSA website (under the Casting Simulation Niyama Criterion Qualification link). Once users obtain the CAD files, they can import them into their simulation software. The website also contains step-by-step instructions regarding how the simulation must be conducted, in order to remove variability caused by many of the user settings in casting simulation packages. Only solidification is to be simulated, in order to eliminate the variability that would be introduced by filling simulations. The sand type, mold-metal interfacial heat transfer coefficient, initial temperatures, and Niyama criterion evaluation temperature are all specified in the instructions as well.

Utilizing the required settings, users then perform their simulation and produce a Niyama contour plot for the casting plane specified in the instructions. The location of this casting plane is shown in Fig. 29a, and an example Niyama plot for this location (the CD3MN benchmark result) is shown in Fig. 29b. Users must then find the minimum Niyama value in this plot, as illustrated in Fig. 29b. Users are instructed to select a Niyama scale that allows the minimum Niyama value in this plot to be determined with a resolution of at least 0.1 $(°C\text{-}s)^{1/2}$ /mm, and then to determine the range into which the minimum Niyama value falls in the contour plot. If the simulation software package utilizes Niyama units other than $(°C\text{-}s)^{1/2}$ /mm, users are instructed to convert their values to these units. Once the range containing the minimum Niyama value has been identified, users must enter the upper limit of this range at the appropriate location in the Simulation Qualification Record form (see Appendix A). For the example shown in Fig. 29b, the value to enter on the form is Ny_{min} = 0.1 $(°C\text{-sec})^{1/2}$ /mm. In addition to entering the minimum Niyama value from their simulation into the Simulation Qualification Record, users also enter the corresponding benchmark minimum Niyama value for that alloy (determined from the Benchmark Results), along with several details regarding the simulation and the alloy thermophysical properties that were used in the simulation. Users then submit this completed form, along with their Niyama contour plot, for qualification.

In order to determine whether or not the simulation for a given alloy is qualified, the user results (in the Simulation Qualification Record and the accompanying Niyama contour plot) are

compared to the benchmark Niyama result for that alloy. If the minimum Niyama value obtained in the qualification simulation is lower than or equal to the benchmark value, then the practitioner is qualified for that alloy. Otherwise, the practitioner is not qualified for that alloy. Having a minimum Niyama value lower than the benchmark value indicates that more shrinkage porosity is predicted in the simulation qualification result than in the benchmark result. In other words, the simulation is conservative compared to the benchmark, and hence is acceptable.

The qualification procedure developed in this study allows one to gain confidence in a user's capability to properly set up and perform a casting simulation, as well as in the user's casting simulation software package and the alloy thermophysical property database for which qualification is being sought. It is important to note that this simulation qualification procedure is intended to be used in addition to current quality assurance methods (radiography, etc.), not as a replacement for these techniques. Niyama criterion results calculated from a solidification simulation can predict only solidification shrinkage porosity. The Niyama criterion cannot predict gas porosity, hot tears, inclusions, etc. Therefore, even a qualified or validated simulation procedure cannot be expected to replace sound engineering judgment or careful casting examination.

8. Conclusions

In the present study, alloy thermophysical property databases, necessary to perform casting simulations, were developed for five commonly used corrosion-resistant alloys: super-austenitic stainless steel CN3MN, duplex stainless steels CD3MN and CD4MCuN, and nickel-based alloys CW6MC and N3M. Plate casting trials were performed for these alloys, in order to record metal and mold temperatures during the solidification and subsequent cooling of the plates. Initial thermophysical property datasets were generated using thermodynamic simulation software. The initial property datasets were then modified using an inverse procedure, which utilizes comparison between measured temperature and cooling rate data with corresponding simulated values to direct changes in the thermophysical properties, until satisfactory agreement between simulated and measured temperatures was reached. Primarily, this involved changing the predicted latent heat and the solidification path of all the alloys. It was also necessary to modify the effective specific heat curves for CD3MN, CD4MCuN and N3M, in order to correctly account for solid-state transformations in these alloys. The same inverse procedure was also used to determine the simulation pouring temperature. Once the pouring temperatures and the alloy property datasets were properly adjusted, good agreement was seen between measured and simulated temperature and cooling rate curves. Once these new datasets were finalized, Niyama criterion contours from the casting trial simulations were compared to the corresponding radiographs, it was seen that the areas on the radiographs with visible shrinkage correspond to regions where the Niyama values are less than $1.0 - 2.0$ (°C-sec)$^{1/2}$ /mm. This range is in agreement with findings from similar studies with other steel and nickel-based alloys.

In addition, a simulation qualification procedure has been developed that can be utilized to determine the validity of a simulation user's Niyama criterion results. The goal of this procedure is to develop sufficient confidence in a user's Niyama criterion results that purchasers may specify minimum Niyama values in critical casting areas, as an additional means ensuring casting soundness in these areas (in conjunction with other commonly quality assurance measures). A password-protected SFSA website (the user ID and password may be obtained by

SFSA members) is now available that contains the qualification procedure, the benchmark results against which the qualification simulation is to be compared, and the thermophysical property databases for the alloys that are included in the benchmark results (CD3MN, CD4MCuN, CF8M, CN3MN, CN7M, CW6MC, CW12MW, M35-1, M30C, N3M, and WCB). Users seeking qualification must visit the website, download CAD files for the standard geometry, and perform a solidification simulation according to the step-by-step instructions on the website. The minimum Niyama criterion value that is determined from this procedure is then compared to the benchmark value. If the minimum Niyama value obtained in the qualification simulation is lower than or equal to the benchmark value, then the practitioner is qualified for that alloy. Otherwise, the practitioner is not qualified for that alloy. The qualification procedure developed in this study allows one to gain confidence in a user's capability to properly set up and perform a casting simulation, as well as in the user's casting simulation software package and the alloy thermophysical property database for which qualification is being sought.

Acknowledgements

References

1. E. Niyama, T. Uchida, M. Morikawa, and S. Saito: *AFS Cast Met. Res. J.*, 1982, vol. 7, pp. 52–63.

2. K.D. Carlson, S. Ou, R.A. Hardin, and C. Beckermann, "Development of New Feeding-Distance Rules Using Casting Simulation: Part I. Methodology," *Metall. Mater. Trans. B*, 33B (2002), pp. 731-740.

3. S. Ou, K.D. Carlson, and C. Beckermann, "Feeding and Risering of High Alloy Steel Castings," *Metall. Mater. Trans. B*, 36B (2005), pp. 97-116.

4. K.D. Carlson, S. Ou, and C. Beckermann: "Feeding of High-Nickel Alloy Castings," *Metall. Mater. Trans. B*, 2005, vol. 36B, pp. 843–856.

5. K. Carlson, S. Ou, R. Hardin, and C. Beckermann, "Development of a Methodology to Predict and Prevent Leakers Caused by Microporosity in Steel Castings," *Proc. 55th SFSA Technical and Operating Conference*, Chicago, Illinois, 2001.

6. K.D. Carlson and C. Beckermann, "Use of the Niyama Criterion to Predict Shrinkage-Related Leaks in High-Nickel Steel and Nickel-Based Alloy Castings," *Proc. 62nd SFSA Technical and Operating Conference*, Chicago, Illinois, 2008.

7. J. Miettinen: *Metall. Trans. B*, 1997, vol. 28B, pp. 281-297.

8. J. Miettinen and S. Louhenkilpi: *Metall. Trans. B*, 1994, vol. 25B, pp. 909-916.

9. JMatPro v4.0, Sente Software Ltd., Surrey Technology Centre, 40 Occam Road, GU2 7YG, United Kingdom.

10. W.J. Boettinger, U.R. Kattner, K.W. Moon and J.H. Perepezko: *DTA and Heat-flux DSC Measurements of Alloy Melting and Freezing*, NIST Recommended Practice Guide, NIST Special Publication 960-15, Washington, D.C., 2006.

11. N. Jain, K.D. Carlson, and C. Beckermann: "Round Robin Study to Assess Variations in Casting Simulation Niyama Criterion Predictions," *Proc. 61st SFSA Technical and Operating Conference*, Chicago, Illinois, 2007.

12. *Personal Daq/3005*, Measurement Computing Corporation, 10 Commerce Way, Norton, MA 02766, USA.

13. DASYLab® v8.0, Adept Scientific, Amor Way, Letchworth, Hertfordshire SG6, UK.

14. Nanmac Corp., 11 Mayhew St., Framingham, MA 01702, USA.

15. MAGMASOFT® v4.6, MAGMA GmbH, Kackertstrasse 11, 52072 Aachen, Germany.

Table 1. Casting trial alloy compositions, given in weight percent.

	Alloy	Element (wt. %)					
		C	Mn	Si	P	S	N
Stainless Steels	CN3MN (super-austenitic)	0.03	0.54	0.81	0.005	0.01	0.24
	CD3MN (duplex)	0.02	1.01	0.64	0.018	0.006	0.14
	CD4MCuN (duplex)	0.022	0.76	0.59	0.02	0.001	0.15
Ni-Based Alloys	CW6MC	0.01	0.72	0.71	0.009	0.001	
	N3M	0.004	0.64	0.23	0.007	0.0001	

	Alloy	Element (wt. %)					
		Cr	Ni	Mo	Cu	Cb/Nb	Fe
Stainless Steels	CN3MN (super-austenitic)	20.32	25.07	6.41			46.57 (bal)
	CD3MN (duplex)	22.1	6.35	2.56			67.16 (bal)
	CD4MCuN (duplex)	25.7	5.76	1.84	3.0		62.16 (bal)
Ni-Based Alloys	CW6MC	21.56	60.68 (bal)	9.1		3.73	3.48
	N3M	0.3	66.84 (bal)	31.0			0.98

Table 2. Measured characteristic temperatures during solidification and cooling, along with latent heats.

Alloy	Event	Temperature (°C)	Latent Heat (kJ/kg)
CN3MN	T_{liq}	1387 ± 1	180 ± 5
	$T_{secondary\ phase}$	1380 ± 2	
	T_{sol}	1300 ± 5	
CD3MN	T_{liq}	1455 ± 2	162 ± 5
	$T_{secondary\ phase}$	1447 ± 3	
	T_{sol}	1385 ± 3	
	$T_{fer\text{-}aus\ start}$	1276 ± 3	
CD4MCuN	T_{liq}	1450 ± 3	162 ± 5
	$T_{secondary\ phase}$	1437 ± 4	
	T_{sol}	1368 ± 3	
	$T_{fer\text{-}aus\ start}$	1223 ± 2	
CW6MC	T_{liq}	1324 ± 1	179 ± 5
	$T_{secondary\ phase}$	1306 ± 4	
	$T_{tertiary\ phase}$	1210 ± 2	
	T_{sol}	1177 ± 3	
N3M	T_{liq}	1374 ± 1	158 ± 5
	$T_{secondary\ phase}$	1364 ± 2	
	$T_{tertiary\ phase}$	1284 ± 5	
	T_{sol}	1254 ± 4	
	$T_{solid\text{-}state}$	830 ± 5	

(a) isometric view

(b) side view, no gating except ingate

(c) top view, no gating except ingate
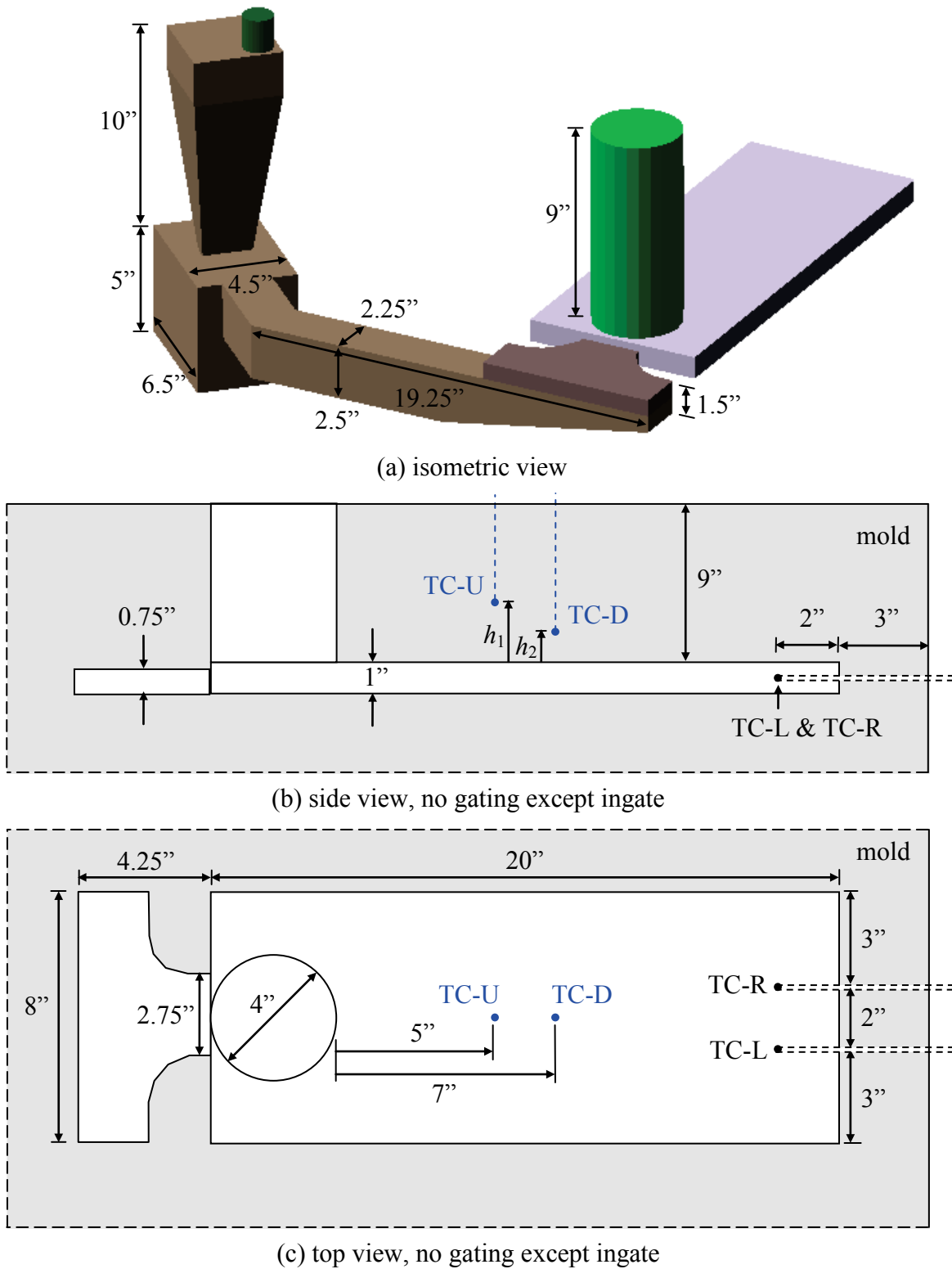
Figure 1.   Schematics of the rigging and thermocouple (TC) arrangement for the plate casting trials. Dashed lines at mold edges indicate the mold continues past the dashed line.
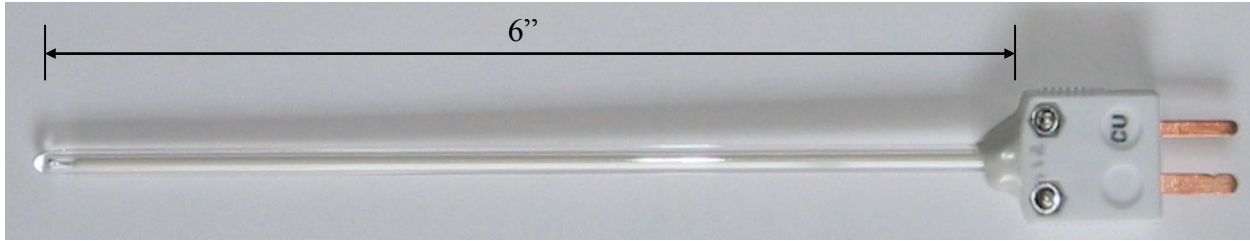
Figure 2.   Photograph of one of the 0.157 in. (4 mm) outer diameter B-type thermocouples employed in the present study.
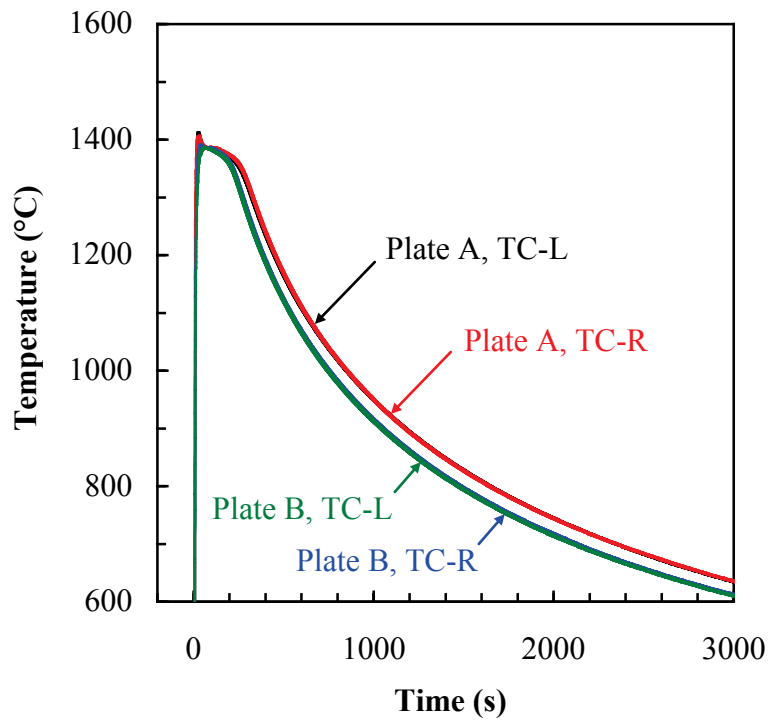
Figure 3.   Thermocouple results for both CN3MN plates.
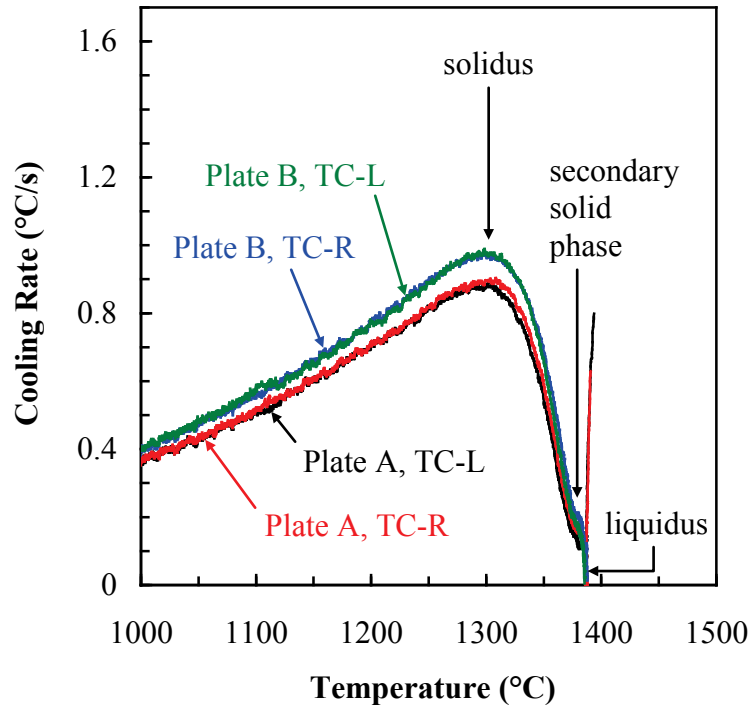
Figure 4.   Cooling rate versus temperature for all four CN3MN thermocouples.
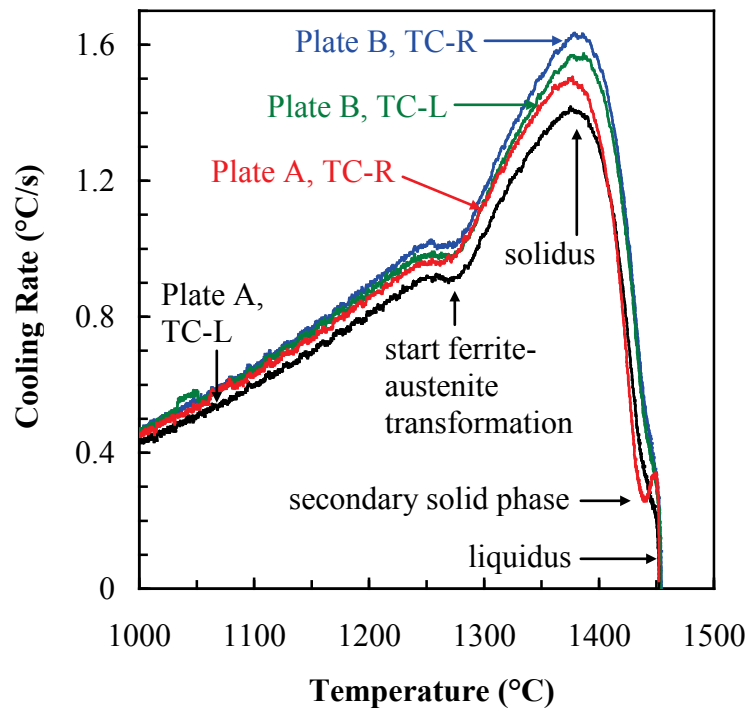
Figure 5.   Cooling rate versus temperature for all four CD3MN thermocouples.
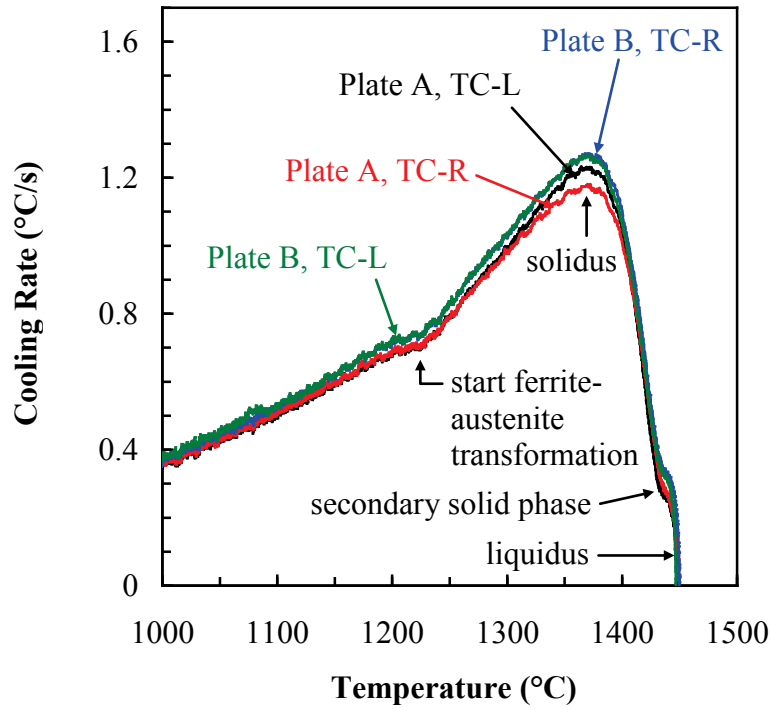
Figure 6.   Cooling rate versus temperature for all four CD4MCuN thermocouples.
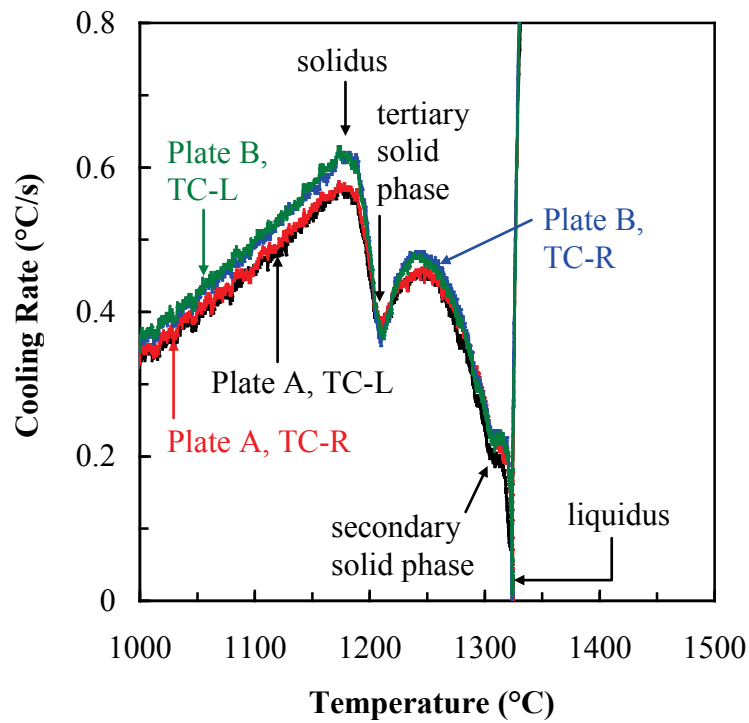
Figure 7.   Cooling rate versus temperature for all four CW6MC thermocouples.
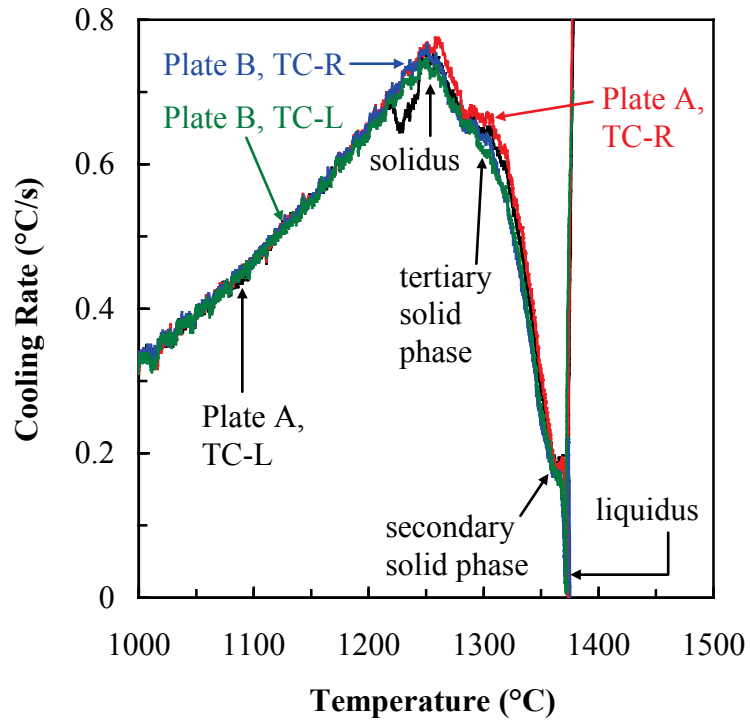
Figure 8.   Cooling rate versus temperature for all four N3M thermocouples.
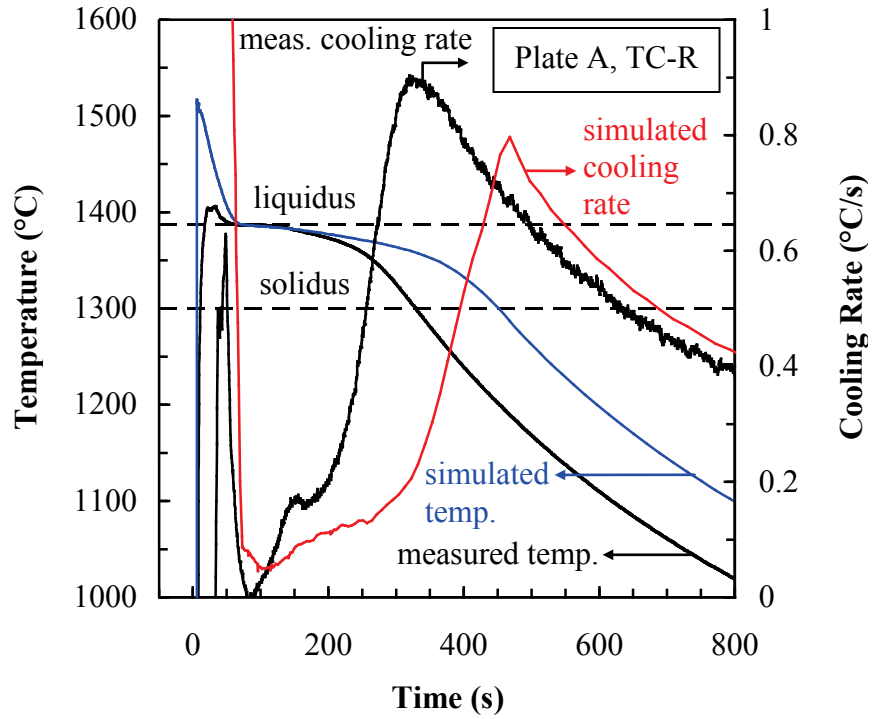
(a) T_{pour} = 1540°C, IDS solidification path and latent heat (L = 253 kJ/kg)
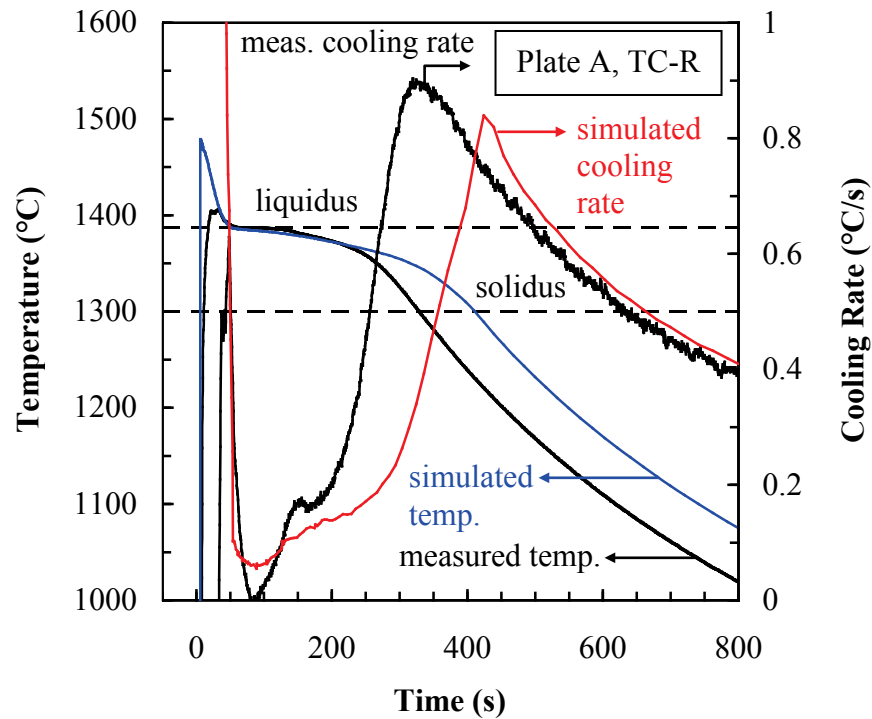
(b) T_{pour} = 1502°C, IDS solidification path and latent heat (L = 253 kJ/kg)

Figure 9.   (see caption on next page)
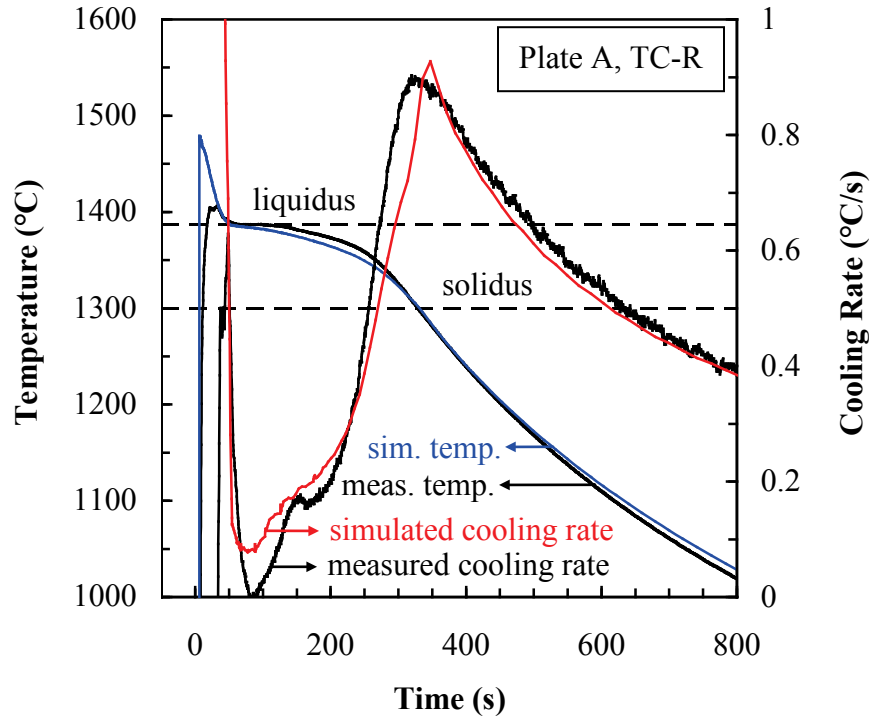
(c) T_{pour} = 1502°C, IDS solidification path, L = 200 kJ/kg
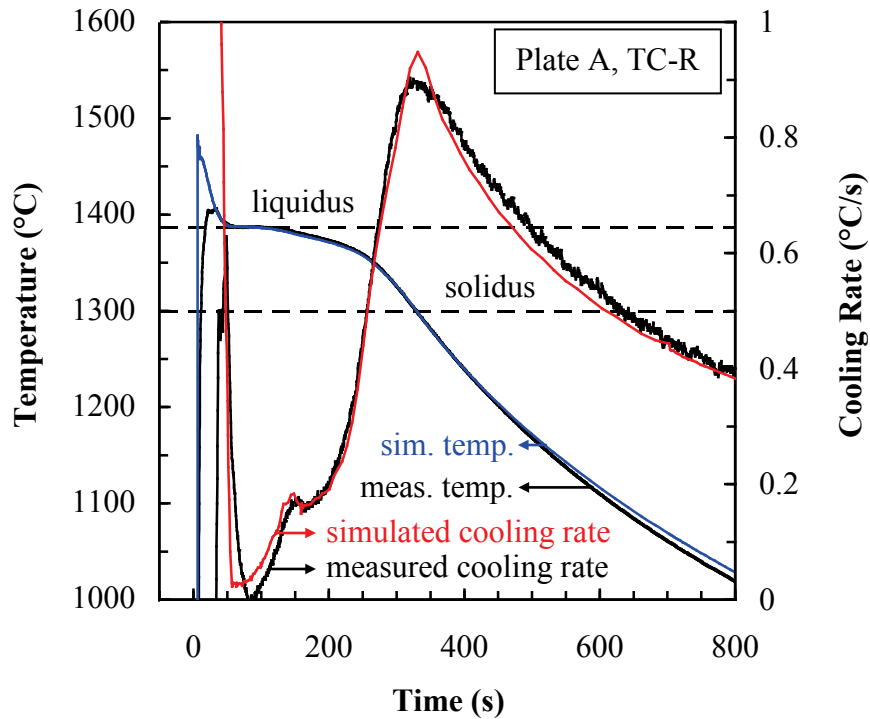
(d) T_{pour} = 1502°C, modified solidification path, L = 180 kJ/kg

Figure 9.   Simulated and measured temperatures and cooling rates for CN3MN simulations using different initial metal temperatures and material properties.
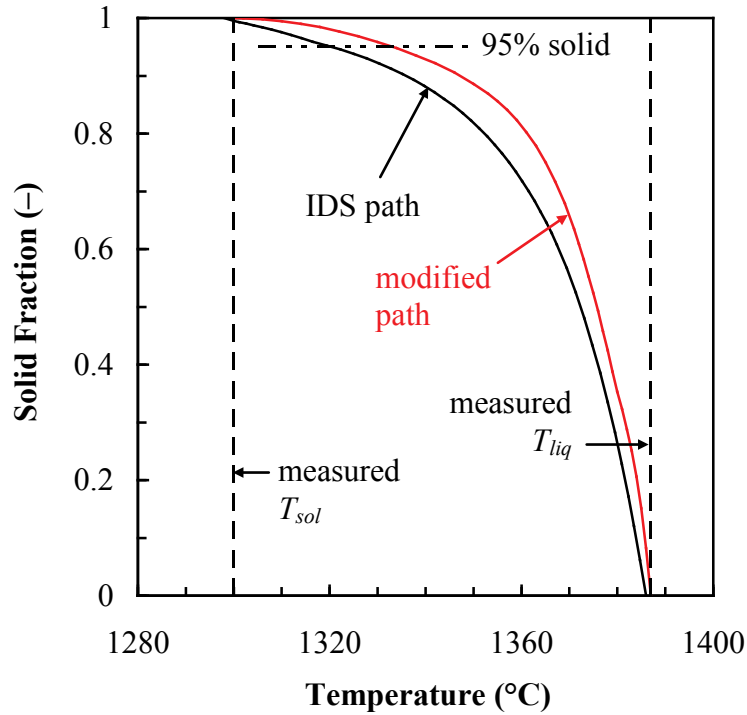
Figure 10. CN3MN solidification path generated by IDS, compared with modified path determined through inverse analysis of thermocouple data.
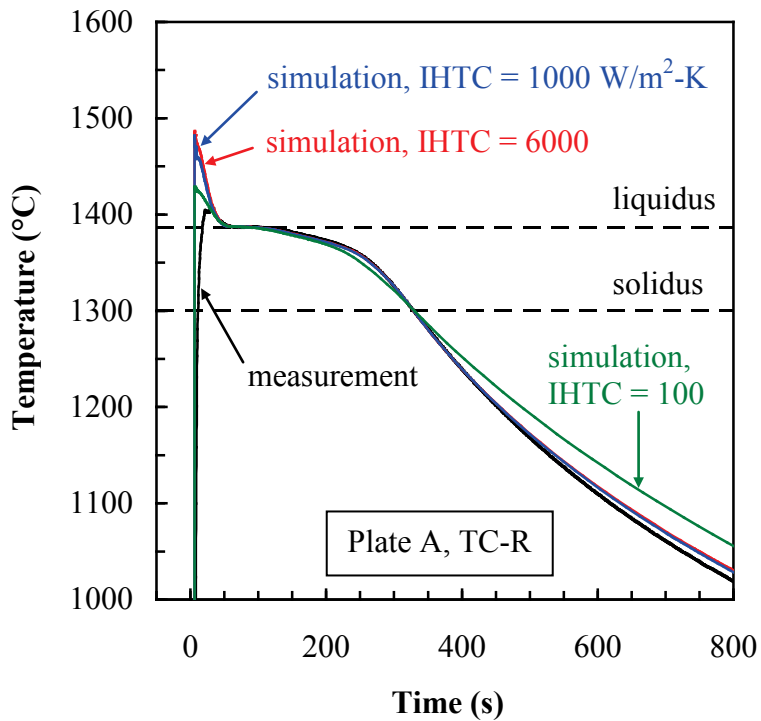
Figure 11. Measured CN3MN temperatures, compared to simulated values computed with different mold-metal interfacial heat transfer coefficients (IHTCs).
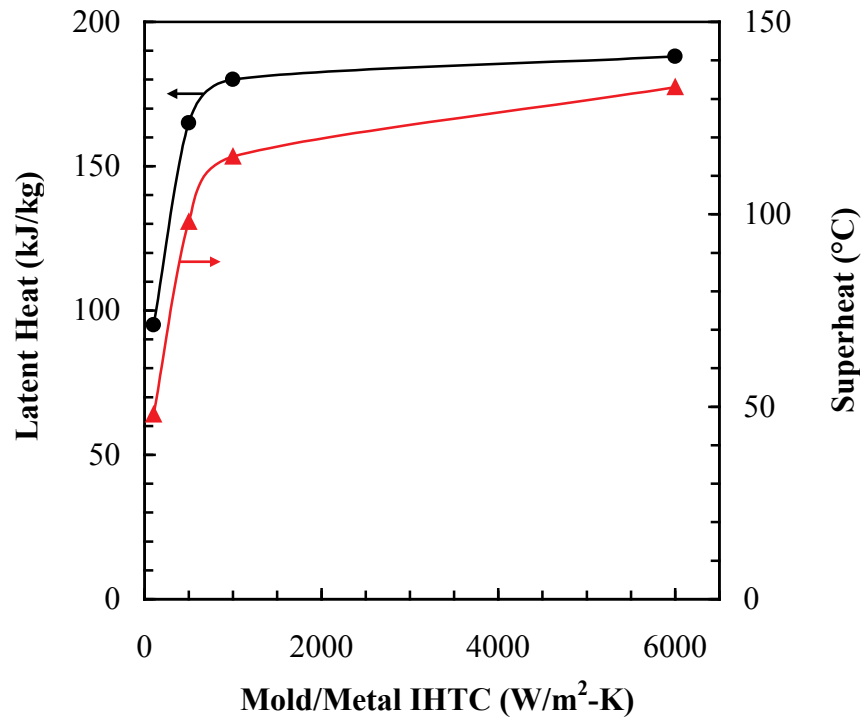
Figure 12. Effect of interfacial heat transfer coefficient (IHTC) on the superheat and latent heat required to achieve agreement between simulated and measured time required to reach liquidus and solidus temperatures in CN3MN Plate A, TC-R.
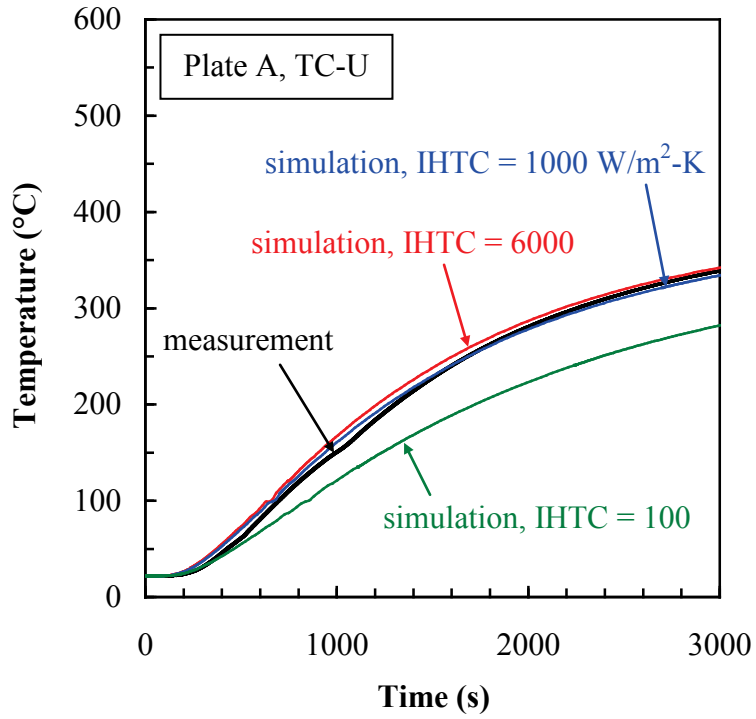
(a) Sand TC 2.0 in. above plate surface
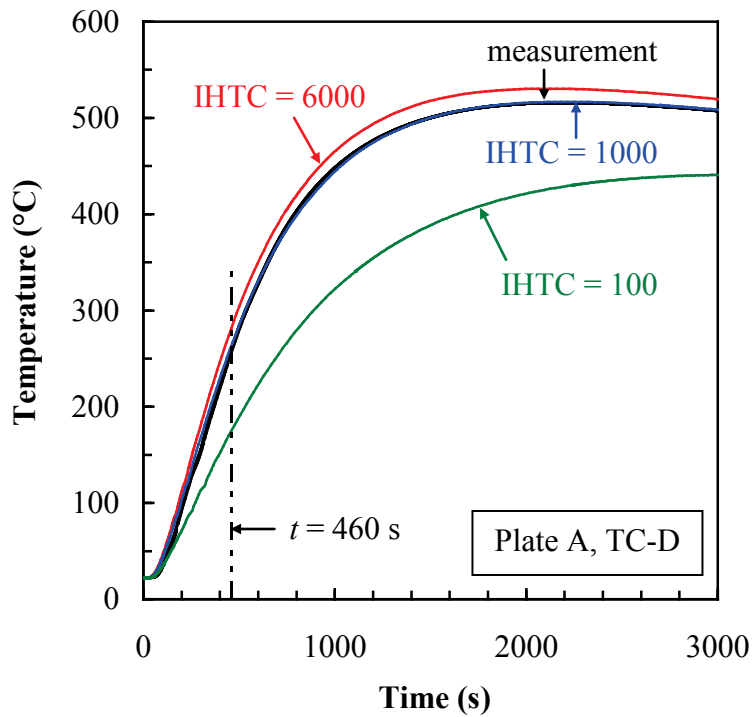
(b) Sand TC 1.1 in. above plate surface

Figure 13.   Measured sand temperatures for CN3MN Plate A mold, compared to simulated values computed with different interfacial heat transfer coefficients (IHTCs).
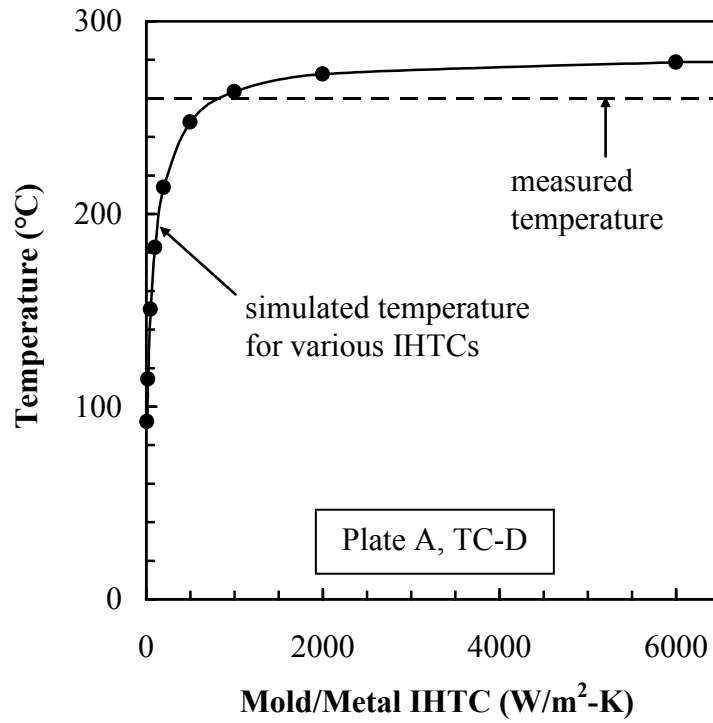
Figure 14. Comparison between measured sand temperature at $t = 460$ s for TC-D in CN3MN Plate A mold and the corresponding simulated temperatures for simulations with various interfacial heat transfer coefficients (IHTCs).
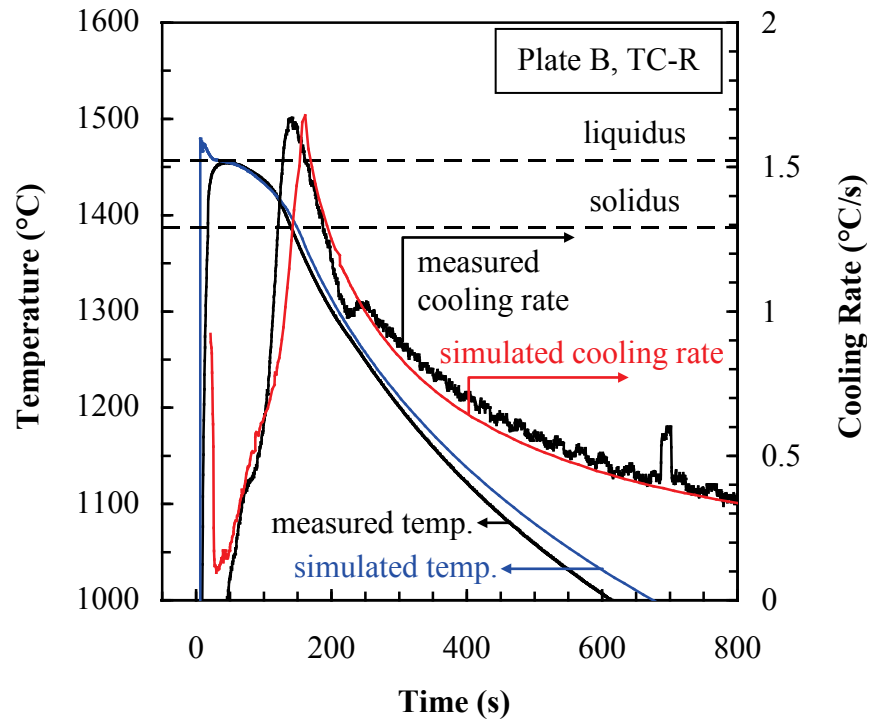
(a) T_{pour} = 1504°C, initial IDS dataset
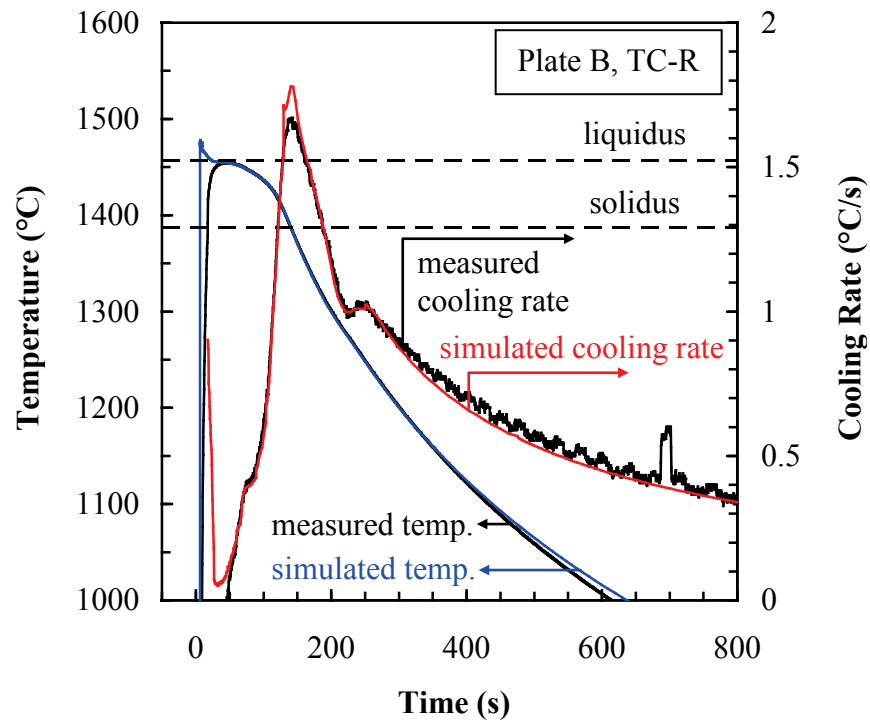
(b) T_{pour} = 1504°C, final modified dataset

Figure 15. Comparison of simulated and measured CD3MN temperatures and cooling rates for Plate B, TC-R, using (a) initial IDS dataset, and (b) final modified dataset.
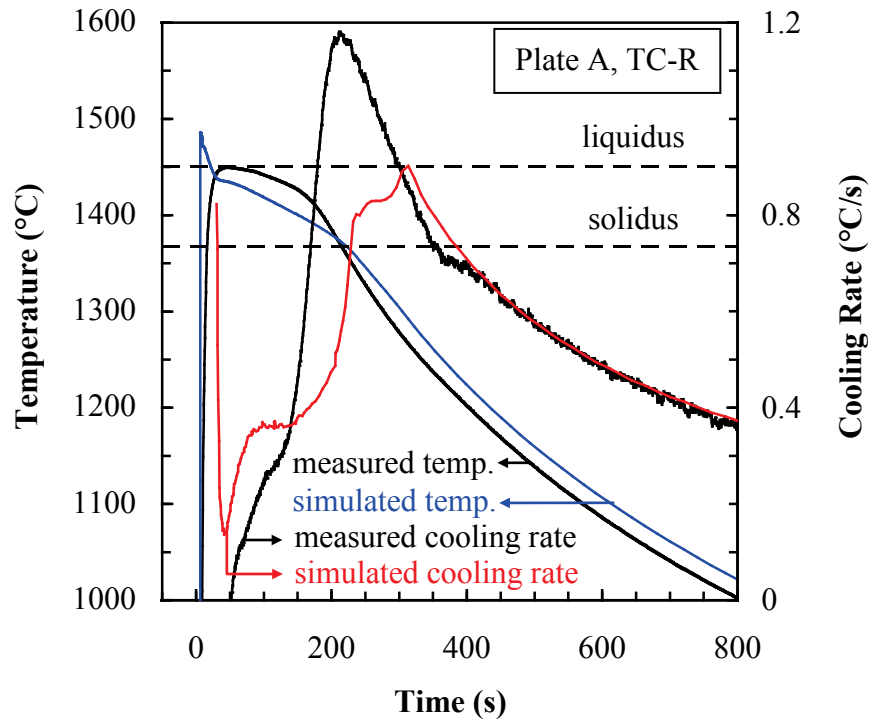
(a) T_{pour} = 1508°C, initial IDS dataset
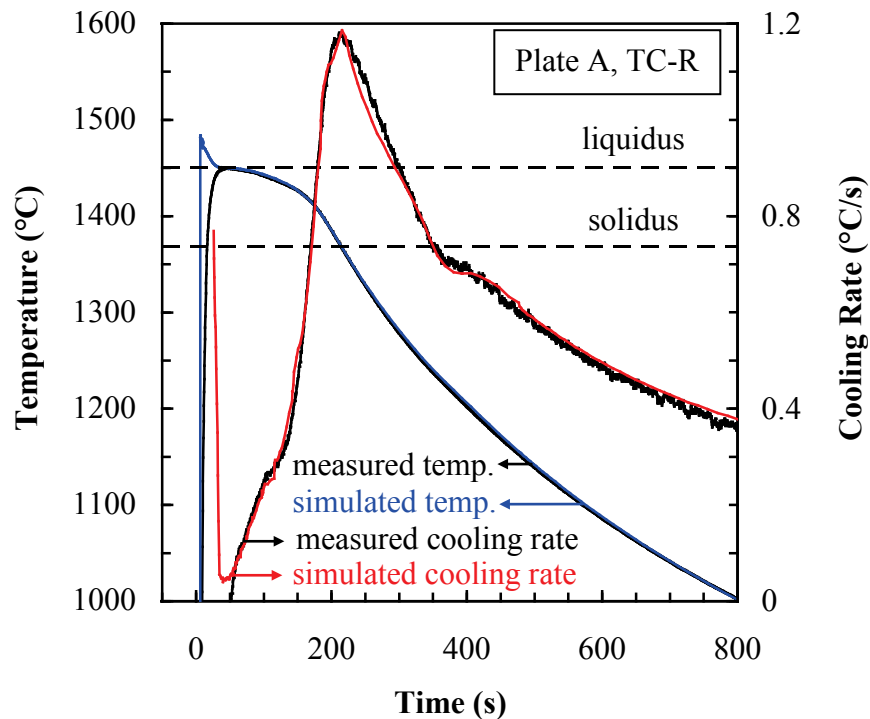
(b) T_{pour} = 1508°C, final modified dataset

Figure 16. Comparison of simulated and measured CD4MCuN temperatures and cooling rates for Plate A, TC-R, using (a) initial IDS dataset, and (b) final modified dataset.
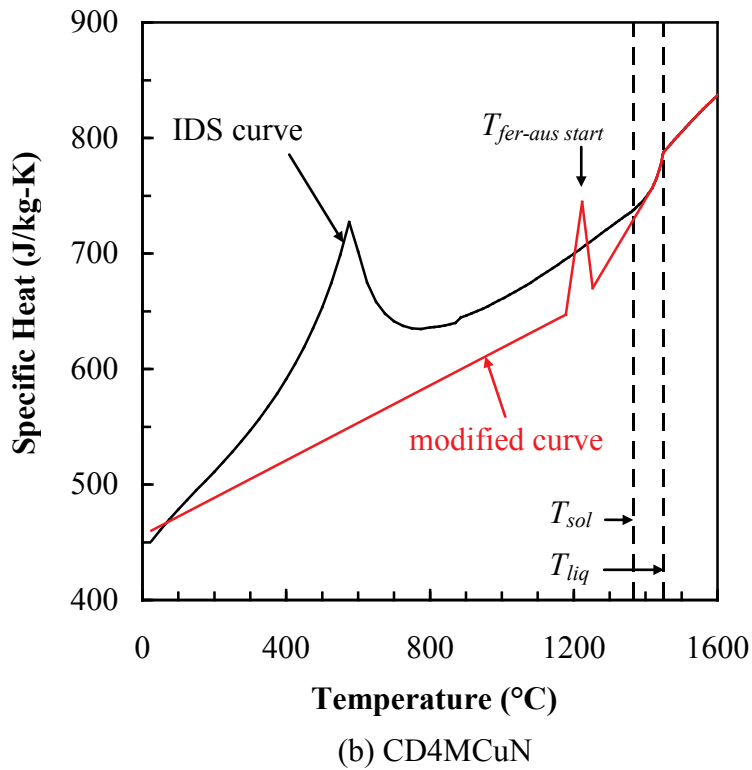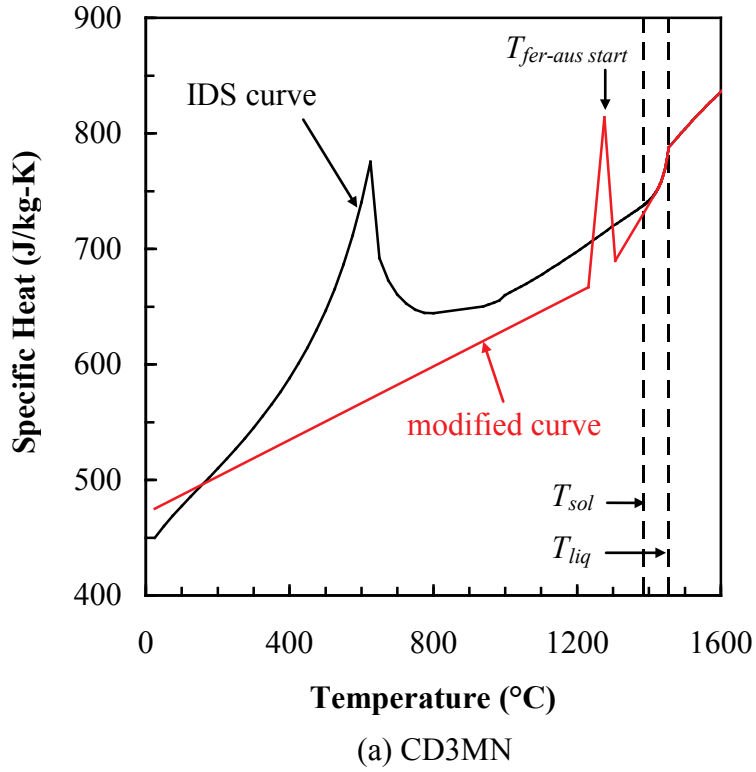
Figure 17. Comparison between original IDS and modified specific heat curves for duplex stainless steels (a) CD3MN, and (b) CD4MCuN.
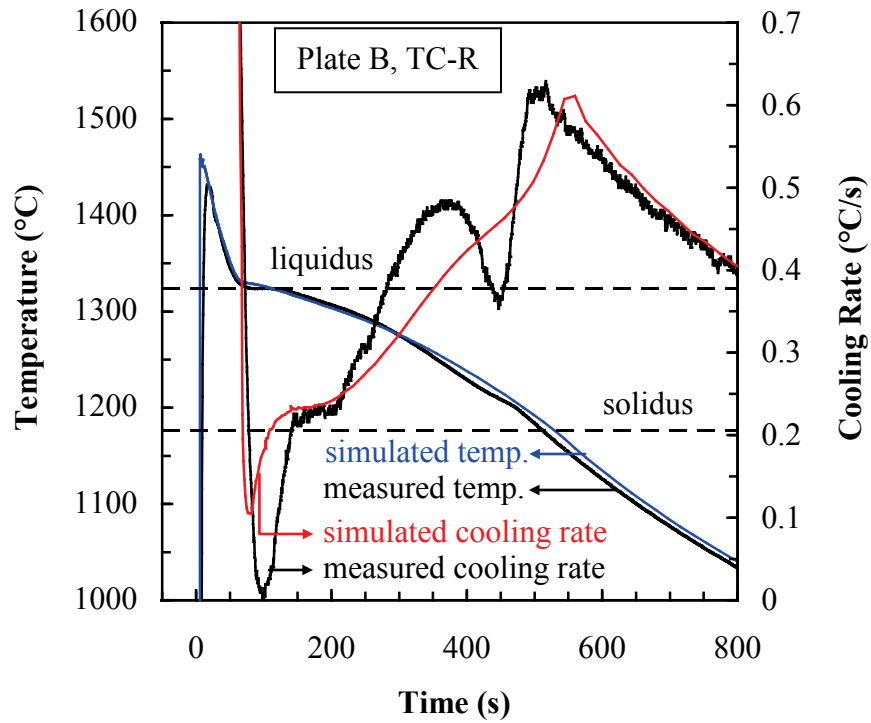
(a) T_{pour} = 1486°C, initial JMatPro dataset
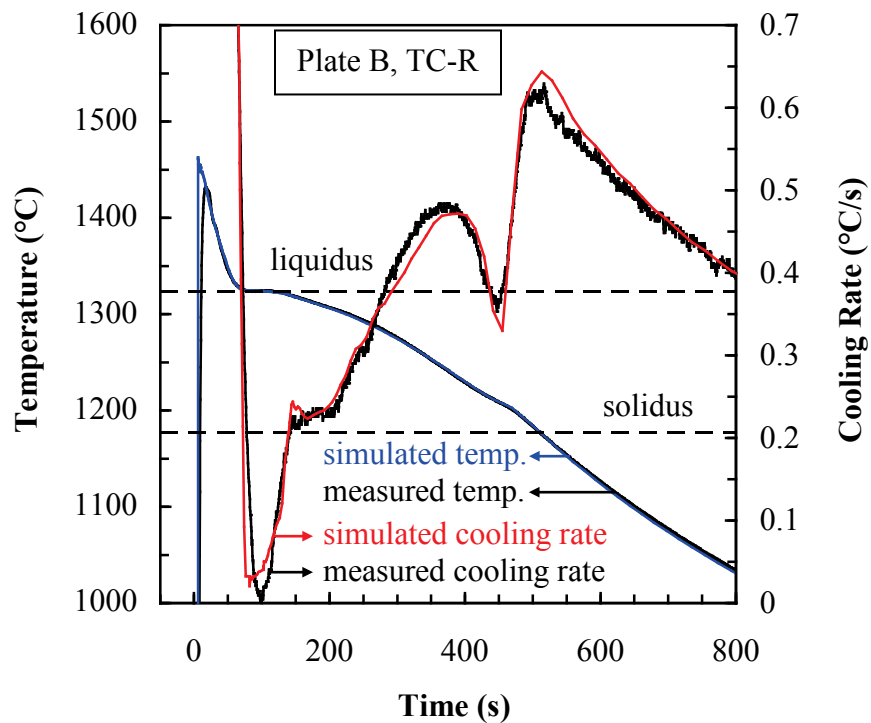
(b) T_{pour} = 1486°C, final modified dataset

Figure 18.   Comparison of simulated and measured CW6MC temperatures and cooling rates for Plate B, TC-R, using (a) initial JMatPro dataset, and (b) final modified dataset.
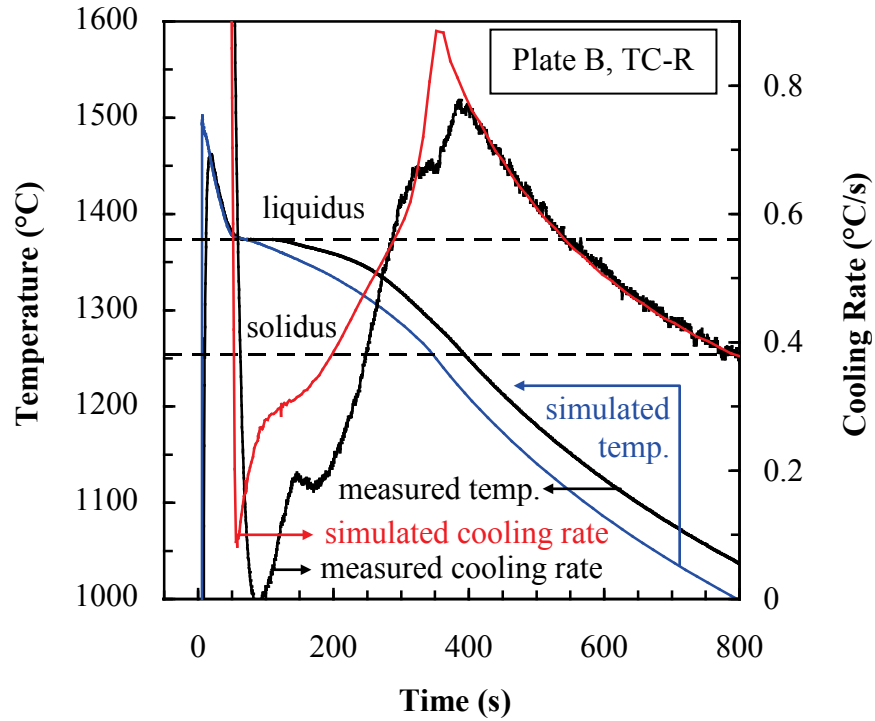
(a) T_{pour} = 1528°C, initial JMatPro dataset
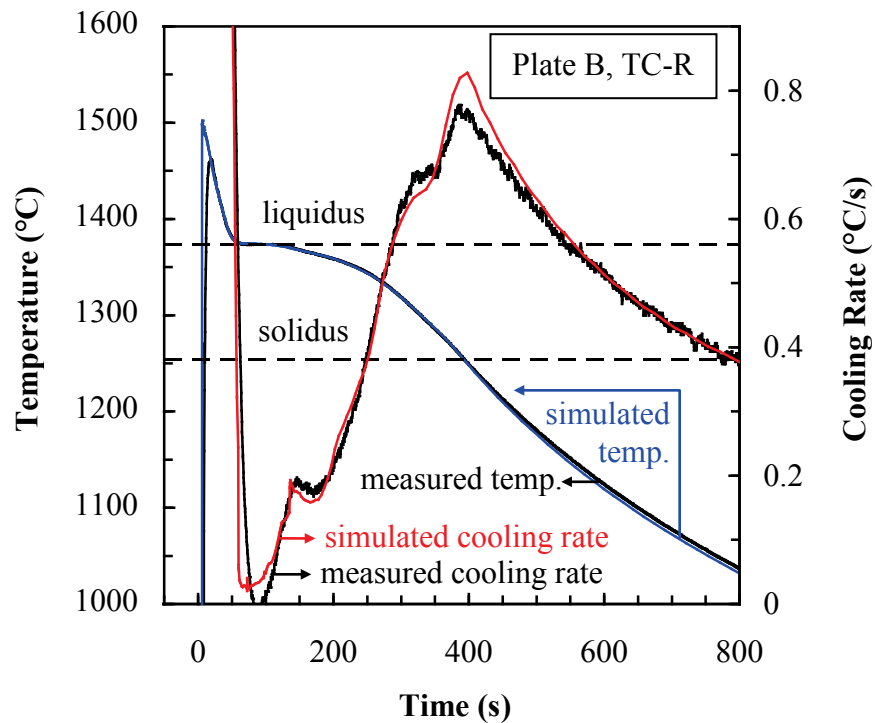
(b) T_{pour} = 1528°C, final modified dataset

Figure 19. Comparison of simulated and measured N3M temperatures and cooling rates for Plate B, TC-R, using (a) initial JMatPro dataset, and (b) final modified dataset.
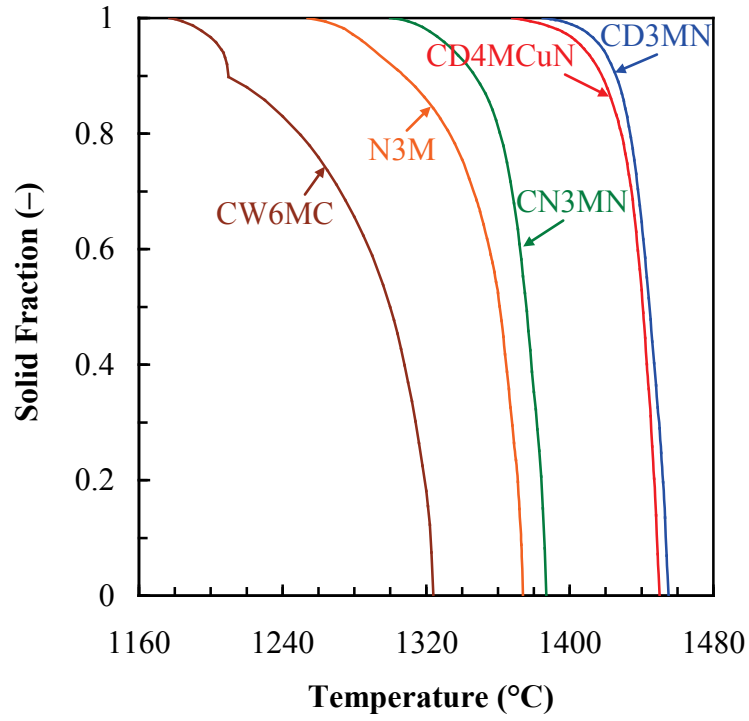
Figure 20. Final solidification paths determined for the five alloys in the present study.
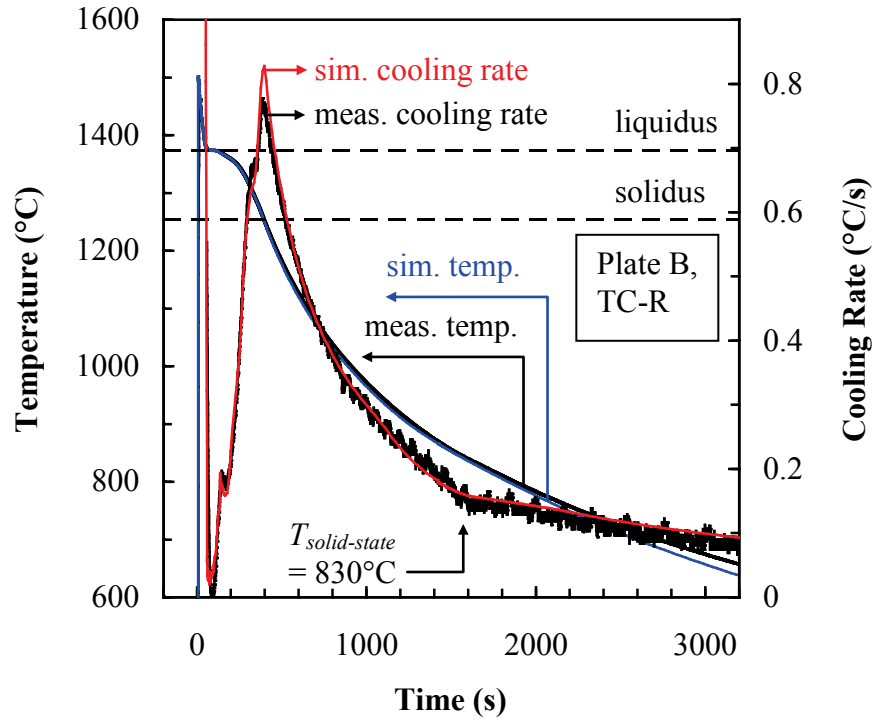
(a) N3M results over long time span
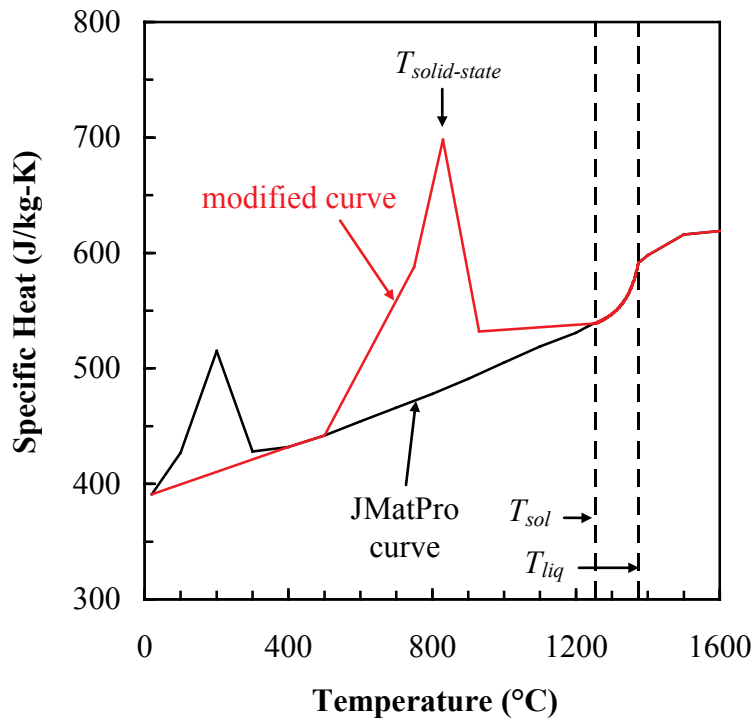
(b) N3M specific heat curves

Figure 21.   (a) N3M results from Fig. 19, shown over a longer time span to include the solid-state transformation; and (b) original and modified specific heat curves.
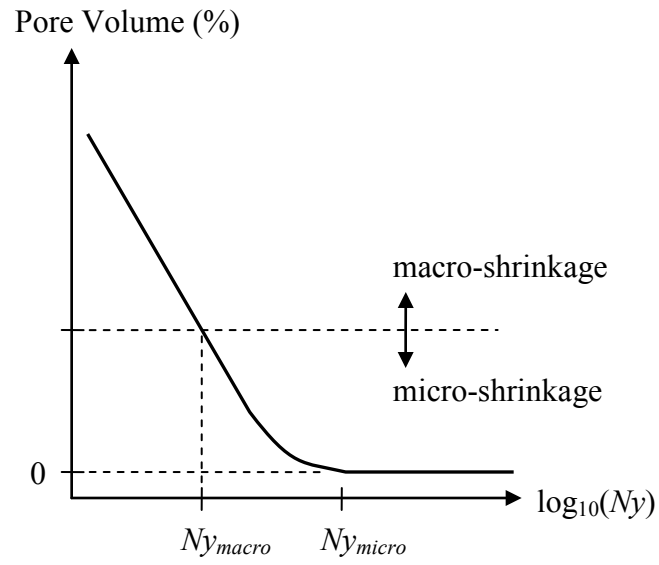
Figure 22. Schematic showing qualitative correlation between Niyama criterion and shrinkage porosity.
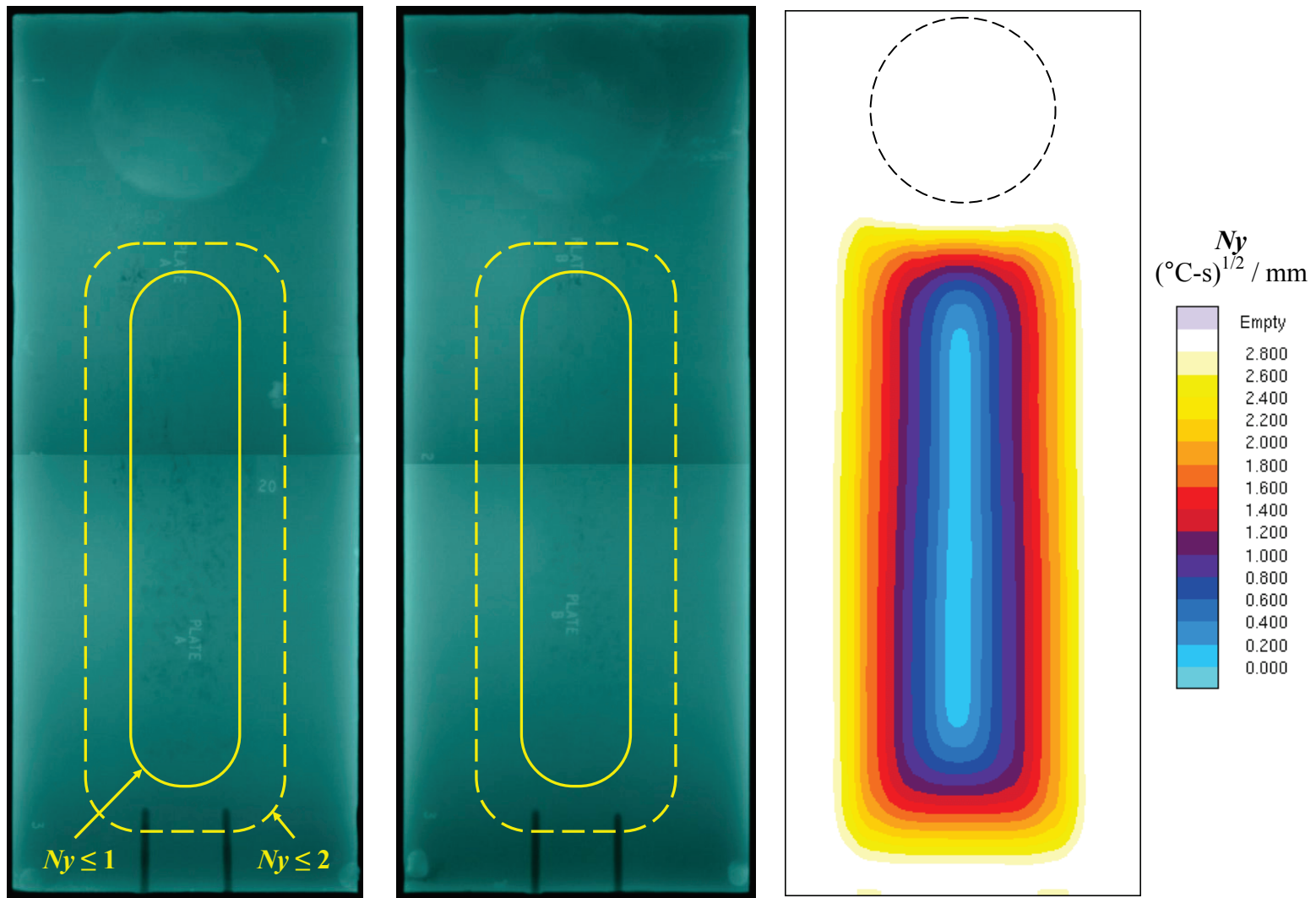
Plate A: CA4, CC3   Plate B: CA2, CC4

Figure 23.   Comparison of the radiographs of both CN3MN plates (ASTM radiographic testing (RT) shrinkage indications listed below each radiograph) with the simulated Niyama criterion contours at the plate mid-plane.
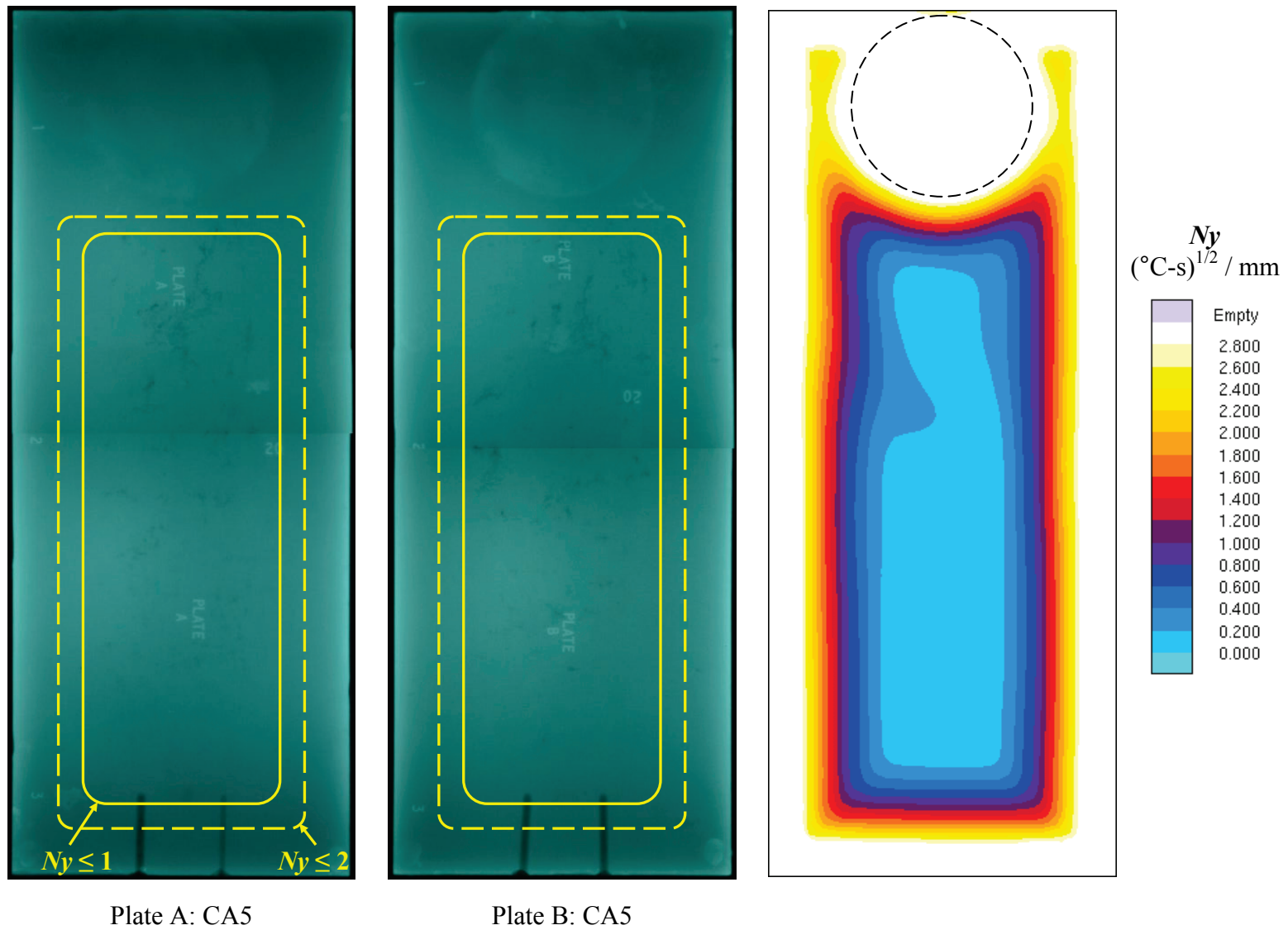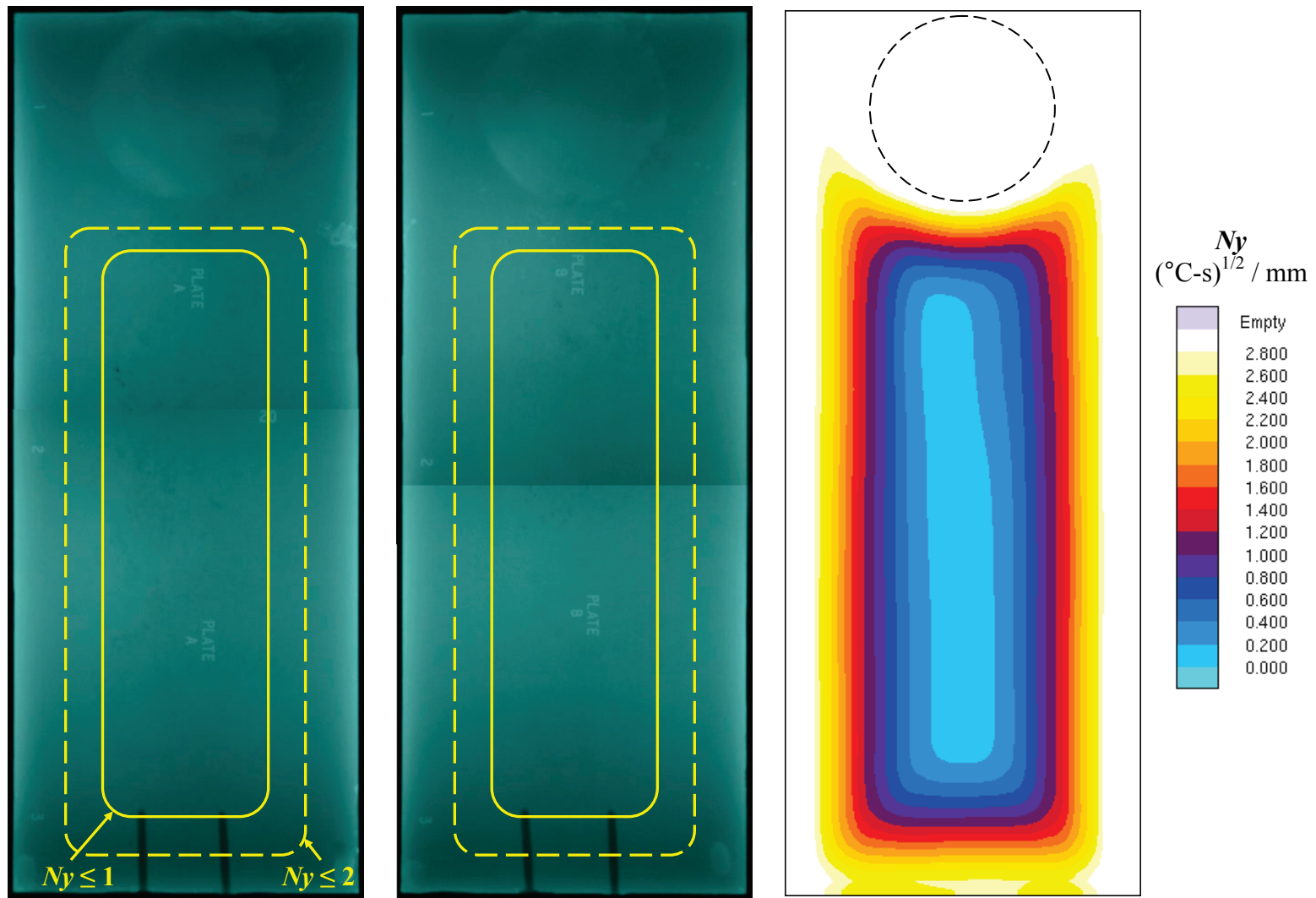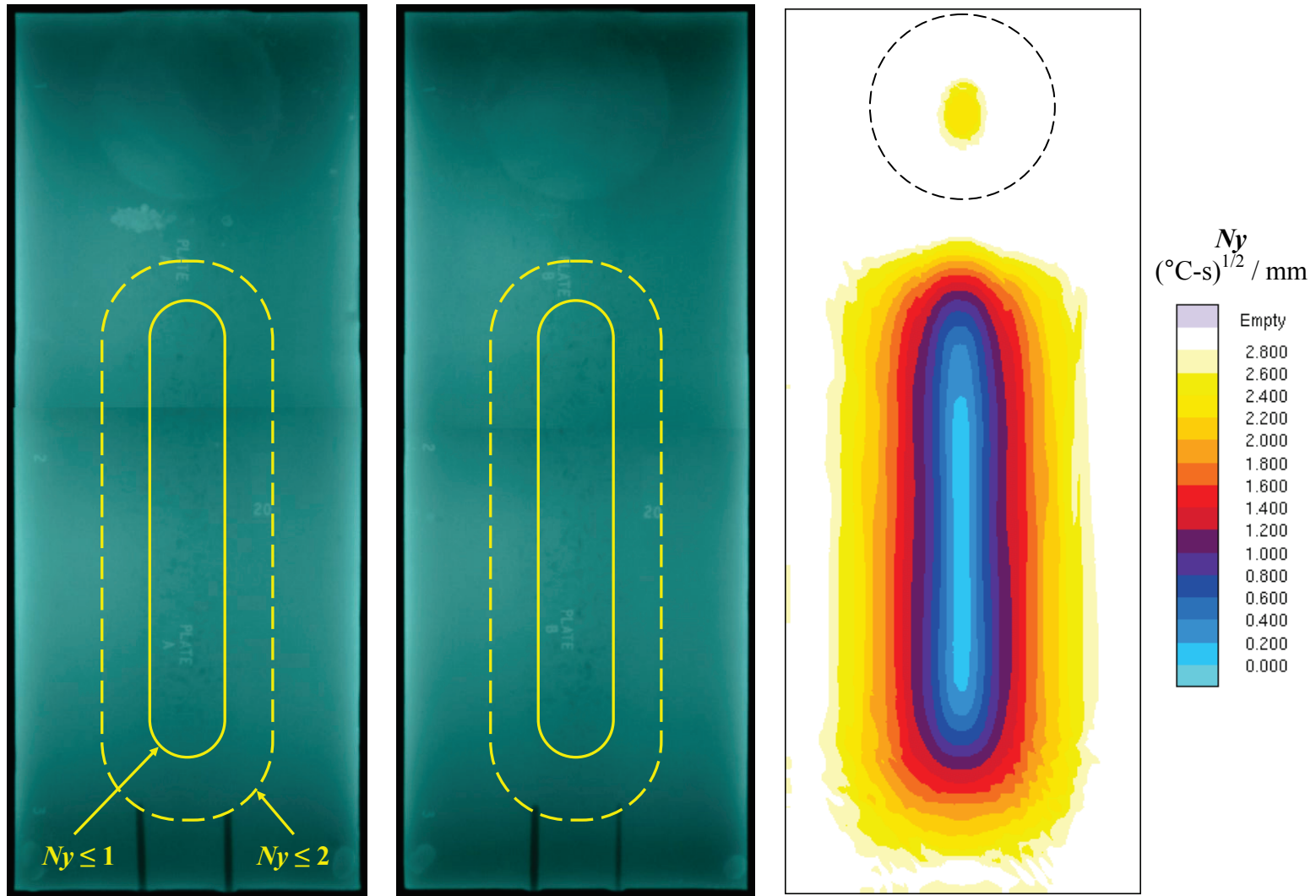
Figure 24. Comparison of the radiographs of both CD3MN plates (ASTM radiographic testing (RT) shrinkage indications listed below each radiograph) with the simulated Niyama criterion contours at the plate mid-plane.

Plate A: CA1, CC5   Plate B: CC4

Figure 25. Comparison of the radiographs of both CD4MCuN plates (ASTM radiographic testing (RT) shrinkage indications listed below each radiograph) with the simulated Niyama criterion contours at the plate mid-plane.
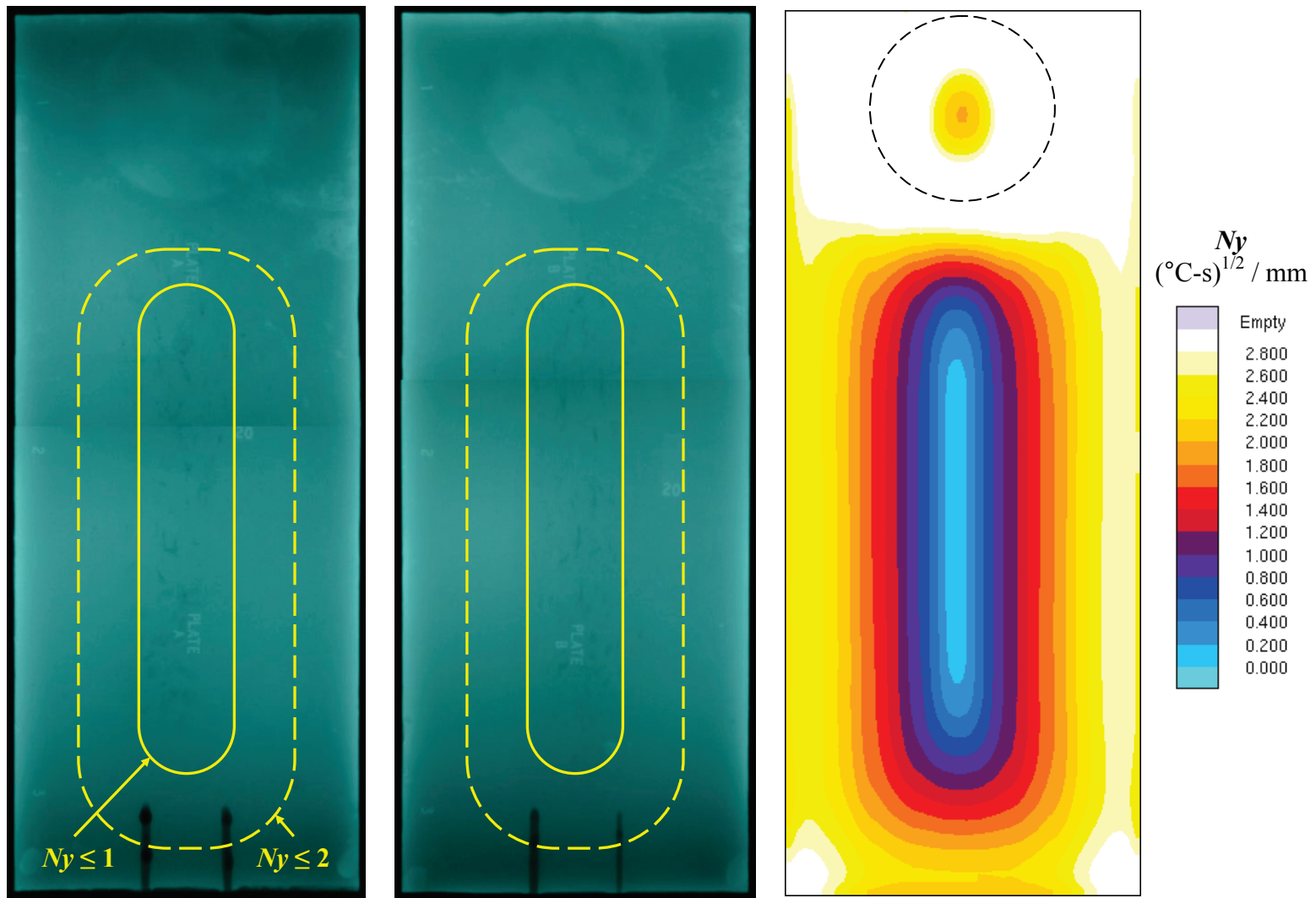
Plate A: CA3, CC4   Plate B: CA5, CC1

Figure 26. Comparison of the radiographs of both CW6MC plates (ASTM radiographic testing (RT) shrinkage indications listed below each radiograph) with the simulated Niyama criterion contours at the plate mid-plane.
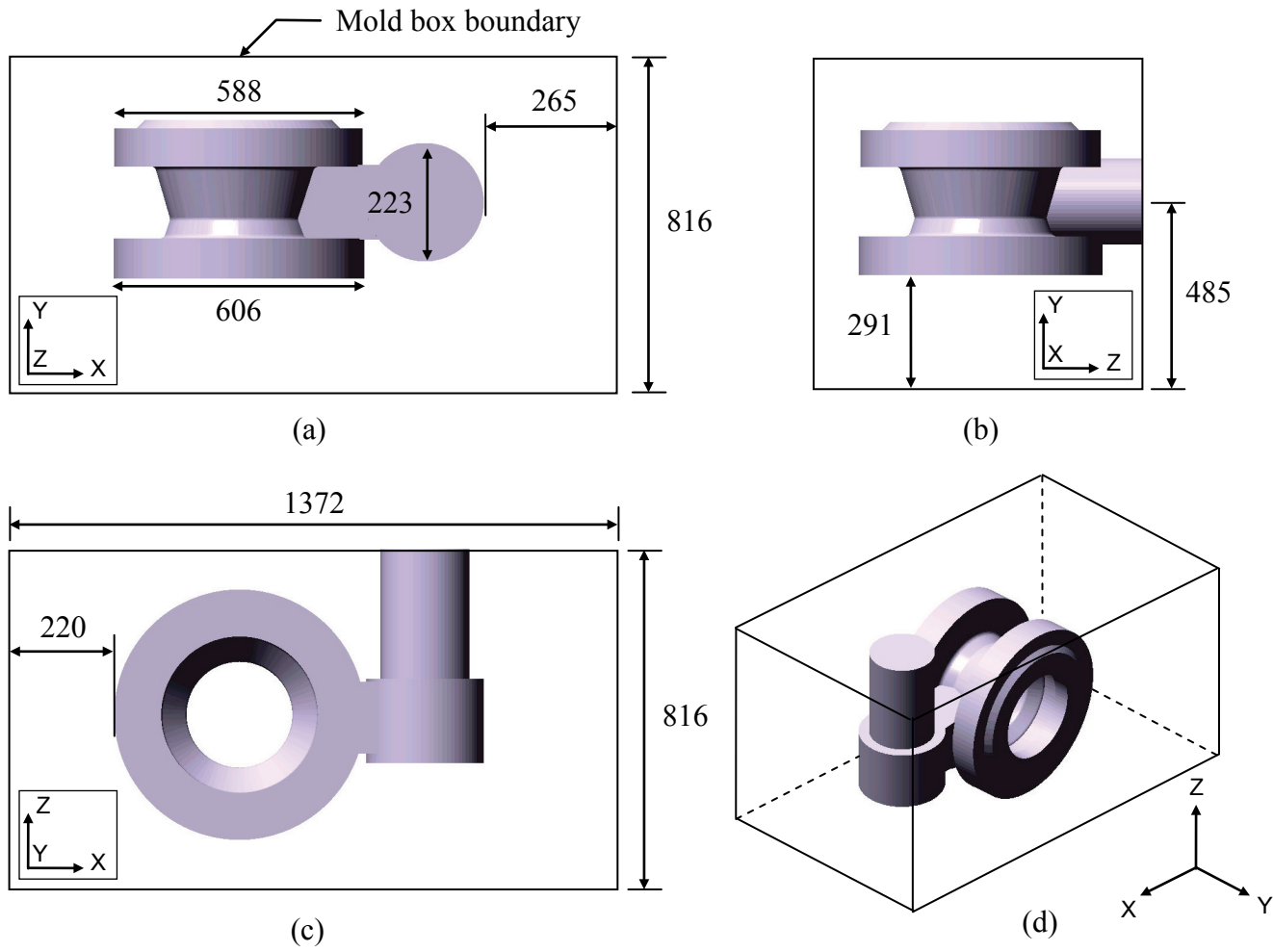
Plate A: CA5   Plate B: CA5

Figure 27.   Comparison of the radiographs of both N3M plates (ASTM radiographic testing (RT) shrinkage indications listed below each radiograph) with the simulated Niyama criterion contours at the plate mid-plane.

Figure 28. Views of the standard simulation geometry. All dimensions are given in mm.
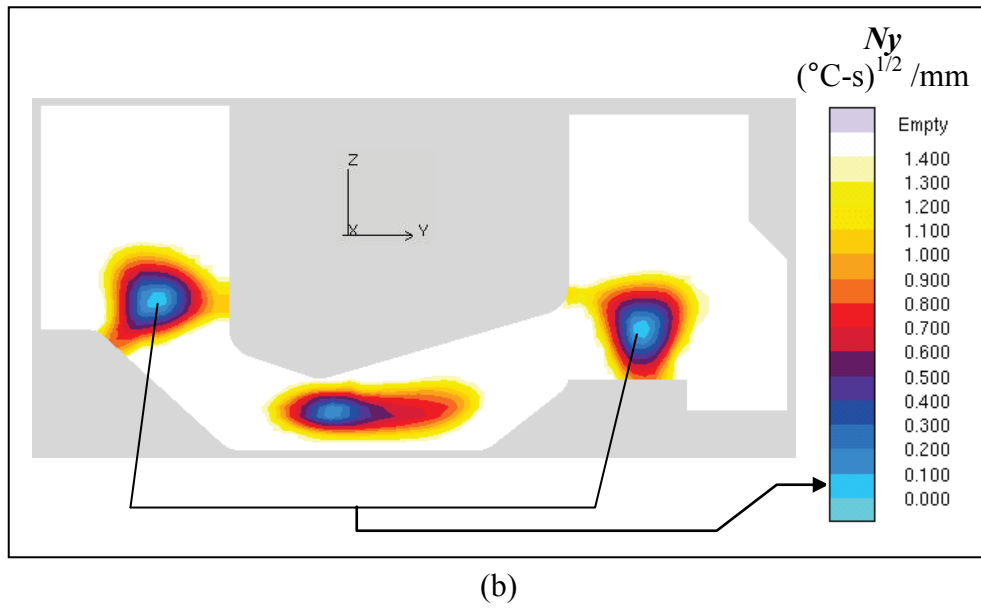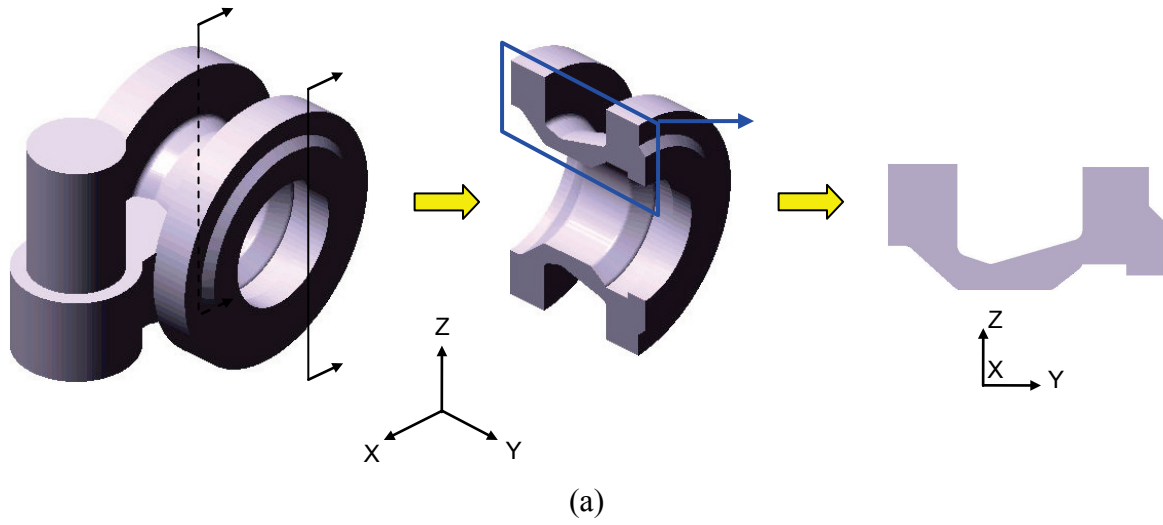
(a)

(b)

Figure 29. (a) Schematic illustrating location of valve cross-section to use for benchmark result, and (b) benchmark result for CD3MN.

Appendix A: Simulation Qualification Record

Simulation Qualification Record

Materials Technology Institute (MTI)
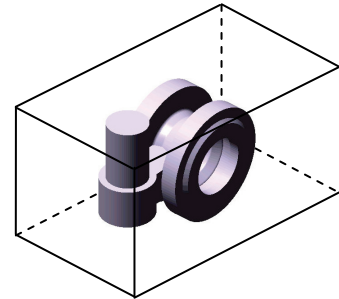Steel Founders' Society of America (SFSA)

Company Name _____   By _____

Simulation Qualification No. _____   Date _____

Name of Alloy Simulated _____

Standard Casting Simulation:
- no filling, solidification only
- furan sand mold, $20^{o}C$
- $100^{o}C$ metal superheat
- mold/metal heat transfer coefficient: 800 W/m^2-K
- $T_{Ny} = T_{sol} + 0.10*(T_{liq} - T_{sol})$

Simulation Details:

	Simulation details
Casting simulation software package used (indicate version)	
Niyama units in your simulation results	
Number of computational cells used (indicate whether your number is number of metal cells or number of total cells)	
Mold properties used (indicate name of database, source and date)	
Metal alloy properties used (indicate name of database, source and date)	
Liquidus temperature, T_{liq} (°C)	
Solidus temperature, T_{sol} (°C)	
Solidification range, [T_{liq} - T_{sol}] (°C)	
Niyama evaluation temperature, T_{Ny} (°C)	

Simulation Results:

Minimum Niyama value obtained [(°C-sec)$^{1/2}$ /mm]:	
Benchmark minimum Niyama value [(°C-sec)$^{1/2}$ /mm]:	

Niyama contour plot attached _____

Approved by:

_____   _____   _____
Simulator   Engineering Manager   QA Manager